Hindawi
International Journal of Aerospace Engineering
Volume 2022, Article ID 2490675, 22 pages
https://doi.org/10.1155/2022/2490675

Research Article

Large-Slenderness-Ratio Supersonic Aircraft Lateral–Directional Coupling Dynamics Analysis and Control

Huitao Lyu,[1] **Zheng Gong**,[1] **Yongliang Chen**,[1] **Wanli Chen**,[2] **and Wenjian Wang**[2]

[1]*College of Aerospace Engineering, Nanjing University of Aeronautics and Astronautics, Nanjing 210016, China*
[2]*Institute of Engineering Thermophysics, Chinese Academy of Sciences, Beijing 100190, China*

Correspondence should be addressed to Yongliang Chen; chenyl79@nuaa.edu.cn

Received 12 May 2022; Accepted 25 August 2022; Published 27 September 2022

Academic Editor: Xianfeng Yang

Large-slenderness-ratio aircraft in which a large portion of the aircraft's mass is concentrated along its centreline face the problem of severe lateral-directional coupling. Previous research has not fully considered the inertia product when conducting stability analyses of such aircraft. However, neglecting the inertia product may threaten the safety of the aircraft during high-speed flight. This paper investigates the effect of the inertia product on the lateral–directional stability. Two methods, one based on eigenstructure assignment (EA) and the other based on an extended state observer (ESO), are developed for the lateral–directional decoupling of a research large-slenderness-ratio aircraft. Simulation results show that both methods can realize decoupling control. The EA-based control achieves better decoupling performance, whereas the ESO-based control has an advantage in terms of disturbance rejection. Finally, the ESO-based attitude controller is validated through a high subsonic flight test. The decoupling and tracking performance of the attitude control demonstrate the effectiveness and practicality of the ESO-based controller.

1. Introduction

High-speed aircraft are faced with the problem of coupling dynamics, especially those configured with a large slenderness ratio (LSR). Historically, these coupling dynamics have resulted in various accidents [1]. In recent years, hypersonic vehicles have experienced rapid development, and an LSR is a common characteristic of these aircraft [2]. To ensure the flight safety of LSR aircraft, stability assessments and control design methods need to be developed.

With large portions of their mass concentrated along the centreline of the airplane, LSR vehicles with symmetric structure often exhibit undesirable stability and control characteristics due to coupling dynamics in the high subsonic, transonic, and supersonic flight regime [1]. The coupling dynamics can be catastrophic in the flight. In order to predict the departure characteristics arising from the coupling dynamics, significant research efforts have been conducted. In 1958, Moul and Paulson [3] proposed the concept of a lateral departure parameter ($C_{n\beta dyn}$) and lateral control departure parameter (LCDP) for high-performance aircraft. In 1966, Lutze et al. [4] presented a unified analytical approach based on the linearized equations of motion for calculating the deviation of departure-predicting parameters. Weissman [5] combined $C_{n\beta dyn}$ with LCDP and divided the plane into areas associated with different departure characteristics. This work gave rise to the "Weissman chart," which is widely used in assessing the departure characteristics of high-speed aircraft [6, 7]. In 2007, Lee et al. proposed a criterion for estimating the optimum lateral static stability margin through experimental research and validated this criterion using flight tests [8]. Previous research has focused on the evaluation and prediction of the lateral–directional stability and departure characteristics of aircraft and has successfully explained the departure phenomenon arising from the coupling dynamics. For symmetric aircraft without the LSR, the inertia product is relatively small compared with the inertia moment around the body roll axis. Therefore, little attention has been paid to the inertia product in the coupling dynamics analysis, and the value of the inertia product

is often ignored in the previous research. However, ignorance of the inertial product in the stability analysis and flight control law design will pose a potential risk to the LSR aircraft flight safety.

Many studies have examined the decoupling control due to the undesired coupling dynamics of aircraft. For example, an adaptive flight control law was developed to enforce performance across all flight conditions of an X-15 aircraft, although the severe disturbance introduced by mechanical nonlinearities and electrical saturation resulted in divergent airplane motions [9, 10]. For the lateral–directional decoupling control of an F-18 with a high angle-of-attack [11], nonlinear dynamic inversion (NDI) in a multivariable system has achieved good decoupling performance. The disadvantage of NDI-based control is that accurate knowledge of the nonlinear dynamics is required [12], but this is very difficult to obtain. To reduce the dependence on the model information, incremental (INDI) was developed to realize three-axis decoupling control of a novel unmanned tiltrotor [13]. For the multiple-input-multiple-output (MIMO) design method based on a linearized model, eigenstructure assignment (EA) exhibits significant advantages in the decoupling control due to the capability of assigning the eigenvalues and eigenvectors simultaneously [14, 15]. The EA-based controller is widely used in lateral–directional decoupling control, especially for tailless aircraft. The decoupled control of a flying-wing aircraft has been achieved under consideration of the necessary flying qualities [16, 17], and EA-based decoupling control has been validated in a wind tunnel [18]. However, EA-based control requires gain scheduling for aircraft with large flight envelopes. In recent years, extended state observer- (ESO-) based controllers [19] have displayed great potential for decoupling control. The decoupling capability of ESO-based control results from treating the coupling dynamics and uncertainties as a disturbance to be estimated and then compensated. For the decoupling attitude control of a hypersonic glide vehicle, Chen et al. [20] used a nonlinear extended observer, which has low storage and computational requirements compared with the traditional gain scheduling. For outer-loop trajectory control, altitude and velocity decoupling control have been achieved with ESO in simulations [21]. Although plenty of simulations have validated the effectiveness of ESO-based control, few high-speed aircraft have been reported to use this control method in real flight tests; thus, the engineering practice of ESO-based decoupling control needs to be further researched and developed.

Faced with the problems of coupling characteristics including the inertial roll coupling, control coupling, Dutch-roll coupling, and so on [1], the lateral–directional dynamics of an LSR aircraft are analyzed considering the inertial product, and then, the decoupling control law is designed. First, the configuration of the research LSR aircraft is described, and the comparison between various coupling-prone aircraft in history and the research LSR aircraft is given which shows the existence of severe coupling characteristics. In addition, a nonlinear model of the lateral–directional coupling dynamics is established. Second, the coupling dynamics are analyzed based on $C_{n\beta dyn}$, LCDP, and the roll-yaw coupling parameter. Different from the previous work above which ignores the inertial product in analysis, the effect of the inertia product is emphasized, and a stability criterion related to the inertia product is firstly derived based on linear analysis. Besides, the control coupling with the inertial product is also dealt with. Third, EA-based MIMO and ESO-based single-input-single-output (SISO) control laws are designed for lateral–directional decoupling control with the hard cross-connection. Fourth, the linear analysis based on the robust control theory of the EA-based controller is performed, and the necessary flying qualities are shown to be satisfied. The Monte Carlo (MC) simulations are conducted and the root-mean-square (RMS) of the tracking error is used to compare the control performance between the ESO-based and EA-based controllers. To further evaluate the disturbance rejection characteristics of the two controllers, gusts of wind are introduced to the simulation. The advantages and disadvantages of the MIMO and SISO design methods are discussed for a better selection of these two methods. Finally, the ESO-based controller is validated in a real flight test. As a result, the proposed control structure can effectively realize decoupling control for high-speed LSR aircraft in engineering practice which provides some new ideas.

The remainder of this paper is organized as follows. The aircraft dynamics model and coupling dynamics analysis are presented in Section 2. The two decoupling control strategies based on EA and ESO are described in Section 3. The simulation results and comparisons with parameter perturbations and wind gusts are presented in Section 4. Section 5 discusses the results of the flight test, while Section 6 states the conclusions to this study.

2. Lateral–Directional Coupling Dynamics Analysis

2.1. Configuration Description. In terms of aircraft design, the lateral static stability of an aircraft is mainly affected by the dihedral and sweep angle of the wing [22].

As depicted in Figure 1, the research LSR aircraft has a large sweep angle, which improves the flight qualities during supersonic flight. In addition, the research LSR aircraft uses ailerons, elevators, and the rudder for roll, pitch, and yaw control, respectively. To increase the moment of inertia around the x-axis, additional weights are attached to the wingtips of the aircraft. The aircraft parameters are summarized in Table 1.

Historically, various aircraft with the LSR configuration have suffered from coupling problems. Table 2 compares the mass properties between several coupling-prone aircraft [1] and the research LSR aircraft considered in this paper.

As shown in Figure 2, the angle of inclination of the principal axis is calculated as [1]

$$\varepsilon = \frac{I_{xz}}{I_{zz} - I_{xx}}. \tag{1}$$

In Table 2, the inclination angle of the research LSR aircraft is between that of the shuttle and the F-100A

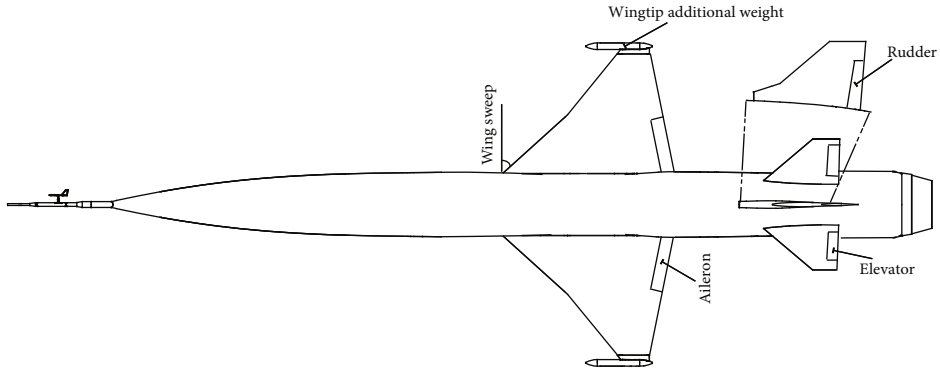

Figure 1: Plan view of the research LSR aircraft.

Table 1: General properties of the research LSR aircraft.

Parameter	Explanation	Value
S	Reference area	1.2 m^2
$\bar{c}$	Mean aerodynamic chord	0.5 m
$\bar{b}$	Wingspan	2.1 m
m	Mass	280 kg
I_{xz}	Product of inertia xz	6 kg·m^2
I_{xx}	Moment of inertia around x-axis	9 kg·m^2
I_{yy}	Moment of inertia around y-axis	300 kg·m^2
I_{zz}	Moment of inertia around z-axis	320 kg·m^2

aircraft. The former experienced control coupling and Dutch-roll coupling during the entry phase, while the latter had serious problems with inertia roll coupling. The value of $(I_{zz} - I_{xx})/I_{yy}$ among all these coupling-prone aircraft is around 1 because I_{xx} is relatively small and I_{yy} and I_{zz} have very similar values. The value of I_{xz}/I_{xx} is 0.67 for the LSR aircraft, which is greater than the equivalent value of all other aircraft in Table 2 except for the X-3. In 1954, the X-3 aircraft showed a series of unexpected, extremely violent motions while testing rudder-fixed aileron rolls. Note that the LSR aircraft has the maximum value of I_{zz}/I_{xx}, which is about twice that of the X-3. The coupling dynamics of the research LSR aircraft must be taken into consideration because the poor mass properties may cause coupling problems.

2.2. Lateral–Directional Cross-Coupled Dynamics. The nonlinearities induced by the pitch motion are ignored in the lateral–directional coupling dynamics because of the small angle-of-attack over the whole flight mission. Compared with longitudinal motion, the lateral–directional dynamics of the research LSR aircraft are more complicated due to the complex inertial and aerodynamic interactions. For flight safety, the instability and divergence of the lateral–directional modes should be analyzed in the high-subsonic and transonic flight regimes [23], where the center-of-pressure position changes dramatically under the unsteady flow field [24]. Based on computational fluid dynamics (CFD), an accurate aerodynamic model is built using a high-dimensional linear interpolation table. In terms of the inertial parameters, the nonlinear lateral–directional dynamic equations are [25]

$$\begin{aligned}
\dot{\beta} &= \frac{Y}{mV} + (p\sin\alpha - r\cos\alpha),\\
\dot{p} &= \frac{(I_y - I_z)I_z - I_{xz}^2}{I_xI_z - I_{xz}^2}rq + \frac{(I_x - I_y + I_z)I_{xz}}{I_xI_z - I_{xz}^2}pq + \frac{I_z}{I_xI_z - I_{xz}^2}L + \frac{I_{xz}}{I_xI_z - I_{xz}^2}N,\\
\dot{r} &= \frac{I_x(I_x - I_y) + I_{xz}^2}{I_xI_z - I_{xz}^2}pq - \frac{(I_x - I_y + I_z)I_{xz}}{I_xI_z - I_{xz}^2}rq + \frac{I_{xz}}{I_xI_z - I_{xz}^2}L + \frac{I_x}{I_xI_z - I_{xz}^2}N,\\
\dot{\phi} &= p + \tan\theta(q\sin\phi + r\cos\phi),
\end{aligned} \tag{2}$$

where L, M, and N are the roll, pitch, and yaw moments induced by the aerodynamic forces, respectively; p, q, and r are the angular velocity for the body roll, pitch, and yaw axes; α and β are the angle-of-attack and the sideslip angle, respectively; ϕ, θ, and ψ are the roll, pitch, and yaw Euler angles, respectively; Y is the side force acting on the aircraft; and V is the true airspeed. The main feature of Equation (2) is that the roll and yaw dynamics are severely coupled with each other. The coupling dynamics are composed of aerodynamic coupling, control coupling, motion coupling, and inertial coupling [7]. Based on the small disturbance theory, the nonlinear model in Equation (2) is linearized using a small deviation. The linearized equation is [25]

$$\begin{bmatrix}\dot{\beta}\\ \dot{p}\\ \dot{r}\\ \dot{\phi}\end{bmatrix} = \underbrace{\begin{bmatrix}\bar{Y}_\beta & \sin\alpha + \bar{Y}_p & \bar{Y}_r - \cos\alpha & g\cos\frac{\theta}{V}\\ \bar{L}_\beta & \bar{L}_p & \bar{L}_r & 0\\ \bar{N}_\beta & \bar{N}_p & \bar{N}_r & 0\\ 0 & 1 & \tan\theta & 0\end{bmatrix}}_{A_{lat}}\begin{bmatrix}\beta\\ p\\ r\\ \phi\end{bmatrix} + \underbrace{\begin{bmatrix}\bar{Y}_{\delta_a} & \bar{Y}_{\delta_r}\\ \bar{L}_{\delta_a} & \bar{L}_{\delta_r}\\ \bar{N}_{\delta_a} & \bar{N}_{\delta_r}\\ 0 & 0\end{bmatrix}}_{B_{lat}}\begin{bmatrix}\delta_a\\ \delta_r\end{bmatrix}, \tag{3}$$

where g is the gravitational acceleration; δ_a and δ_r are the aileron and rudder deflection angles, respectively; A_{lat} is the system matrix; and B_{lat} is the control input matrix. The parameters of the moments and forces induced by the sideslip angle, roll angular rate, and yaw angular rate are defined as

Table 2: Mass properties of coupling-prone aircraft [1].

Aircraft	X-15	X-3	Shuttle	FY-102	F-100A	The research LSR aircraft
m (kg)	455	680	6154	944	745	280
I_{xx} (kg·m^2)	3600	4100	895000	13200	10976	9
I_{yy} (kg·m^2)	85000	61200	6918000	106000	57100	300
I_{zz} (kg·m^2)	86500	65100	7199000	114600	64975	320
I_{xz} (kg·m^2)	-650	4200	167000	3540	942	6
ε (deg)	-0.45	3.95	1.52	2.00	1.00	1.11
$\frac{I_{xz}}{I_{xx}}$	-0.18	1.02	0.19	0.27	0.09	0.67
$\frac{I_{zz}}{I_{xx}}$	24.03	15.88	8.04	8.68	5.92	35.56
$\frac{I_{yy}-I_{zz}}{I_{xx}}$	-0.42	-0.95	-0.31	-0.65	-0.72	-2.22
$\frac{I_{zz}-I_{xx}}{I_{yy}}$	0.98	1.00	0.91	0.96	0.95	1.04
$\frac{I_{xx}-I_{yy}}{I_{xx}}$	-0.94	-0.88	-0.84	-0.81	-0.71	-0.91

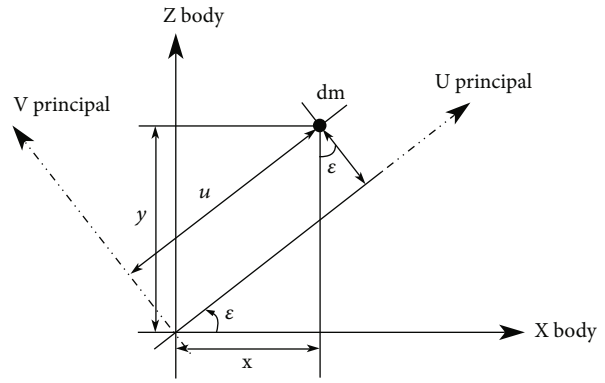

Figure 2: Angle of inclination of the principal axis.

$$\begin{aligned}\bar{Y}_i &= \frac{1}{mV}\frac{\partial Y}{\partial i},\\ \bar{L}_i &= \frac{L_i + (I_{xz}/I_z)N_i}{I_x - I_{xz}^2/I_z},\\ \bar{N}_i &= \frac{N_i + (I_{xz}/I_x)L_i}{I_z - I_{xz}^2/I_x},\end{aligned} \tag{4}$$

where $i \in \{\beta, p, r, \delta_a, \delta_r\}$. For level flight, the assumption that $\theta = \alpha$ can be made.

2.3. Stability and Departure Analysis with Inertial Product. In general, static stability and dynamic stability are considered in the stability and departure analysis [4]. The former requires only the knowledge of aerodynamic characteristics, while the latter requires the linear system defined in Equation (3) to be analyzed. All the dynamic stability criteria based on linear system analysis can be derived using the Routh–Hurwitz stability criterion, based on the coefficients of the characteristic polynomial. For simplicity, the effect of the aerodynamic forces and moments resulting from the angular rates and the acceleration of gravity are disregarded. The simplified system matrix A_s is given as

$$A_s = \begin{bmatrix} \bar{Y}_\beta & \sin\alpha & -\cos\alpha & 0 \\ \bar{L}_\beta & 0 & 0 & 0 \\ \bar{N}_\beta & 0 & 0 & 0 \\ 0 & 1 & \tan\theta & 0 \end{bmatrix}. \tag{5}$$

The characteristic equation of A_s can be written as

$$\lambda^2\left(\lambda^2 - \bar{Y}_\beta\lambda + \bar{N}_\beta\cos\alpha - \bar{L}_\beta\sin\alpha\right) = 0, \tag{6}$$

where λ is the eigenvalue associated with the system matrix. According to the Routh–Hurwitz stability criterion, the stability requirements are

$$\begin{aligned}\bar{Y}_\beta &< 0,\\ \bar{N}_\beta\cos\alpha - \bar{L}_\beta\sin\alpha &> 0.\end{aligned} \tag{7}$$

The first term in Equation (7) naturally holds because the side force coefficient of the sideslip angle $C_{s\beta}$ is negative. The second term can be expanded and simplified as

$$C_{n\beta dyn} = \left(C_{n\beta} + \frac{I_{xz}}{I_{xx}}C_{l\beta}\right)\cos\alpha - \frac{I_{zz}}{I_{xx}}\left(C_{l\beta} + \frac{I_{xz}}{I_{zz}}C_{n\beta}\right)\sin\alpha > 0, \tag{8}$$

where $C_{l\beta}$ and $C_{n\beta}$ are the rolling and yawing static stability parameters for the sideslip angle, respectively. Equation (8)

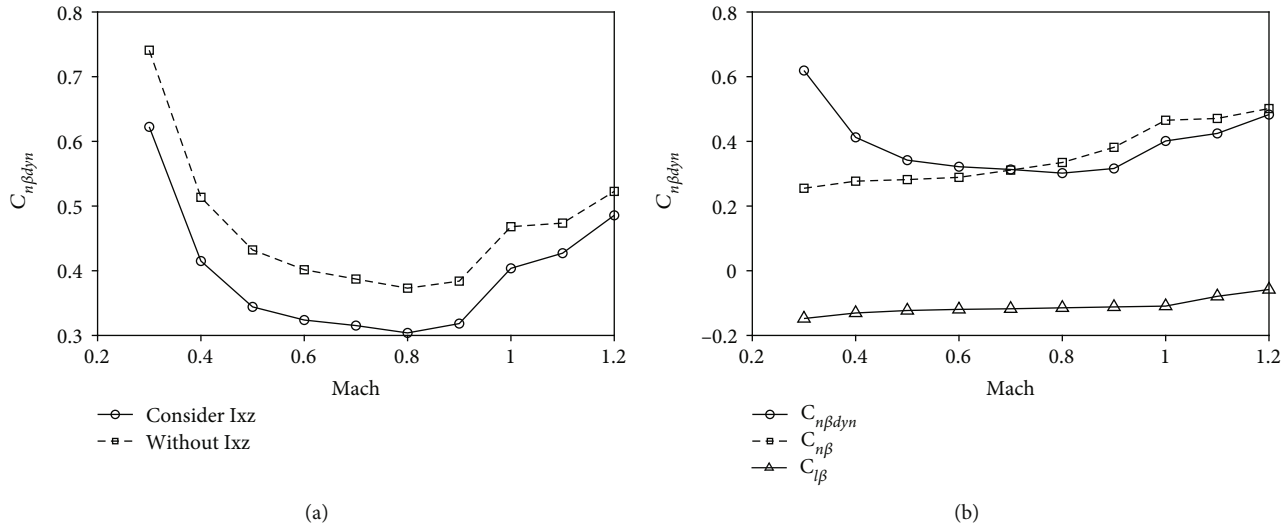

FIGURE 3: Lateral–directional stability parameter with respect to Mach number (at the reference CG position). (a) Analysis of $C_{n\beta dyn}$ with and without I_{xz}. (b) $C_{n\beta dyn}$, $C_{n\beta}$, and $C_{l\beta}$ with respect to Mach numbers.

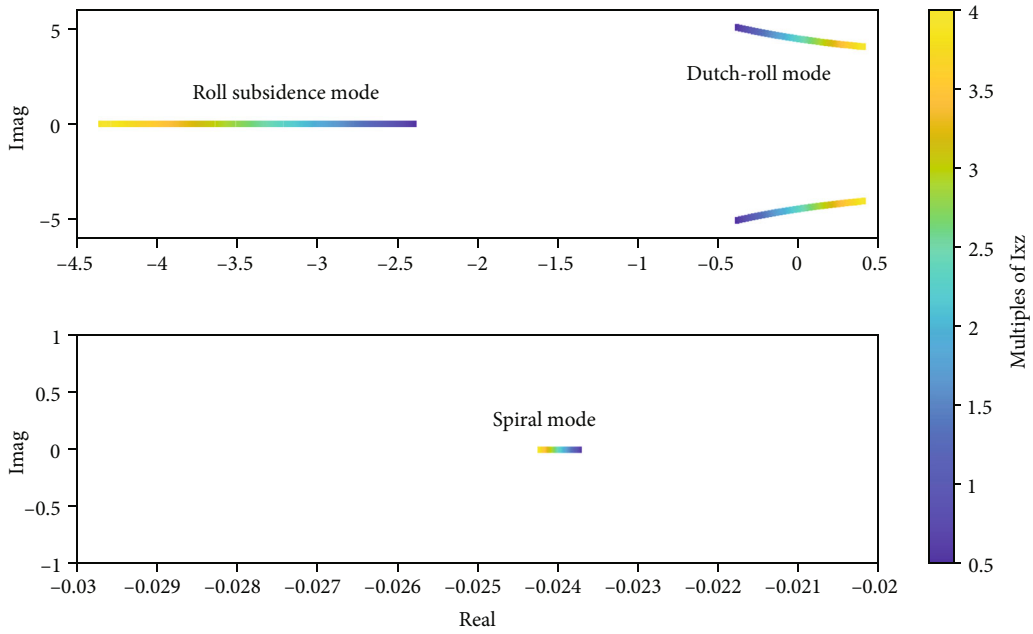

FIGURE 4: Lateral–directional modes change with multiples of I_{xz} (Ma = 0.8).

TABLE 3: Effect of mass properties with and without the WAW.

Condition	I_{xz} (kg·m^2)	I_{xx} (kg·m^2)	I_{xz}/I_{xx}
With WAW	6	9	0.67
Without WAW	10	5	2.0

defines the dynamic lateral–directional stability parameter $C_{n\beta dyn}$. Note that the inertia product I_{xz} has been ignored in previous research; however, neglecting this parameter may introduce a significant bias to the LSR aircraft. The dynamic lateral–directional stability parameter of the research LSR aircraft is calculated along the flight trajectory of the mission, and the center of gravity (CG) position is located at a reference point, as shown in Figure 3(a). There exists an approximate 20% bias in the results when the value of I_{xz} is not introduced, and the results considering I_{xz} are more conservative.

For high-subsonic or transonic flights, the trim value of the angle of attack is quite small, especially for relatively lightweight vehicles such as the research LSR aircraft. The following inequality can be derived from Equation (8):

$$C_{n\beta} + \frac{I_{xz}}{I_{xx}} C_{l\beta} > 0. \tag{9}$$

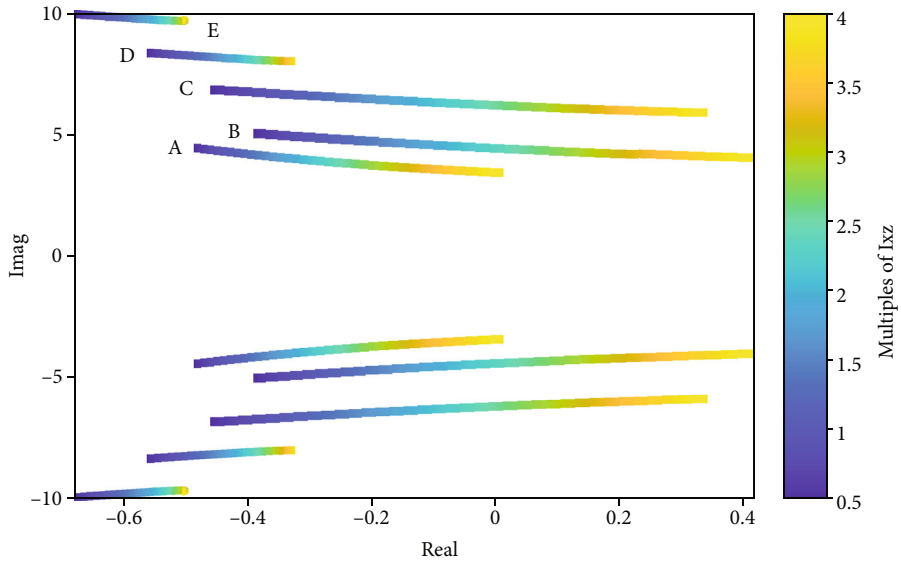

FIGURE 5: Dutch-roll mode changes at multiples of I_{xz} and various Mach numbers (A: Ma = 0.6; B: Ma = 0.8; C: Ma = 1.0; D: Ma = 1.2; E: Ma = 1.4).

As depicted in Figure 3(b), $C_{l\beta} < 0$ and $C_{n\beta} > 0$ for all Mach numbers, confirming the static stability of rolling and yawing aerodynamic performance. Under the small angle-of-attack assumption, the necessary condition for the inertia product so that lateral–directional stability is satisfied can be concluded as

$$I_{xz} < -\frac{C_{n\beta}}{C_{l\beta}} I_{xx}. \tag{10}$$

To further evaluate the effect of the inertia product on the stability of lateral–directional modes, the research LSR aircraft model is trimmed at a steady level-flight condition with an altitude of $H = 10{,}000$ m and a speed of Ma = 0.8. Figure 4 depicts the movement of the eigenvalues at the root locus for the LSR vehicle, where the multiples of the inertia product are in the range 0.5–4.

In Figure 4, the frequency of the Dutch-roll mode decreases with increasing inertia product; in contrast, the frequency of the roll subsidence mode increases. The Dutch-roll mode tends to become unstable as the multiples of the inertia product increases and crosses the imaginary axis at a value of 2.3. Table 3 presents the effect of the wingtip additional weight (WAW) on the mass properties. The value of I_{xz}/I_{xx} is 2.0 without the WAW, which is close to the boundary of stability. Furthermore, the ratio of I_{xz}/I_{xx} is sensitive to the WAW: adding a weight of 2.5 kg results in a threefold increase. Considering the uncertainties of the inertia product, some allowance must be given when designing the aircraft weight distribution.

To evaluate the sensitivity of the Dutch-roll mode to the inertia product in different flight phases, the Dutch-roll mode with respect to changes in the inertia product and Mach number is shown in Figure 5. For the subsonic (Ma < 0.8) and supersonic (Ma > 1.2) flight phases, the Dutch-roll mode is less sensitive to the inertia product and remains stable over the range of multiples considered here. However, the Dutch-roll mode becomes unstable at multiples of around 2 in the transonic phase. The conclusion is that the inertia product should be the focus of attention when analyzing the stability of the Dutch-roll mode in the transonic flight phase.

Another widely used indicator for roll departure susceptibility is the LCDP [26], which can be derived using the roll angle and roll angle rate feedback to the aileron. The closed form of the system matrix A_{cl} with roll angle feedback is

$$A_{cl} = \begin{bmatrix} \bar{Y}_\beta & \sin\alpha_b & -\cos\alpha_b & k\bar{Y}_{\delta_a} \\ \bar{L}_\beta & 0 & 0 & k\bar{L}_{\delta_a} \\ \bar{N}_\beta & 0 & 0 & k\bar{N}_{\delta_a} \\ 0 & 1 & \tan\theta & 0 \end{bmatrix}, \tag{11}$$

where k is the feedback gain. Similar to the derivation process for Equation (6), the Routh–Hurwitz stability criterion in Equation (12) can be established; the detailed derivation is shown in Reference [4].

$$\bar{N}_\beta - \bar{L}_\beta \frac{\bar{N}_{\delta_a}}{\bar{L}_{\delta_a}} > 0. \tag{12}$$

If we retain the inertia product, the inequality can be expanded as

$$\text{LCDP} = \left(C_{n\beta} + \frac{I_{xz}}{I_x} C_{l\beta}\right) - \left(C_{l\beta} + \frac{I_{xz}}{I_z} C_{n\beta}\right) \times \left[\frac{C_{n\delta_a} + (I_{xz}/I_x) C_{l\delta_a}}{C_{l\delta_a} + (I_{xz}/I_z) C_{n\delta_a}}\right] > 0. \tag{13}$$

As shown in Figure 6(a), the LCDP calculated using Equation (13) is about 5% less than the value without the

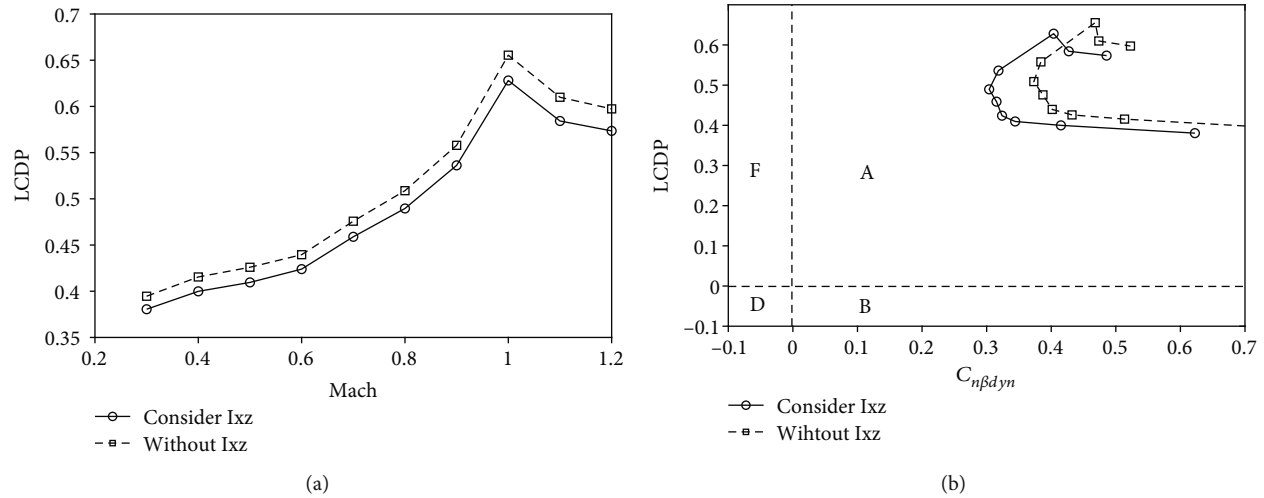

Figure 6: LCDP and Weissman chart analysis results. (a) LCDP results with and without the inertia product. (b) Weissman chart results with and without the inertia product (region A: no departure; regions B–F: increasing departure and spin susceptibility).

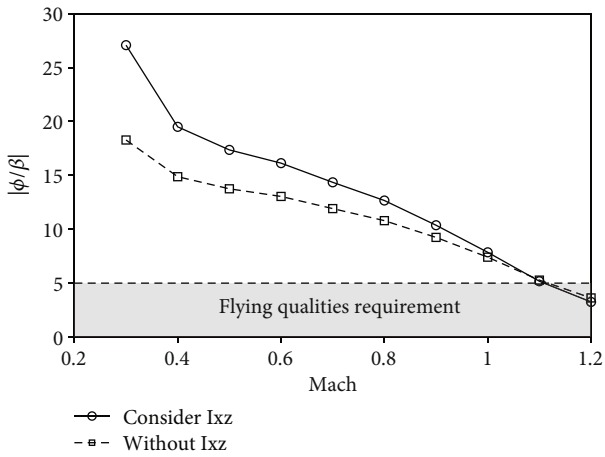

Figure 7: Diagram of roll–yaw coupling.

inertia product. Weissman's chart [6] gives a criterion combining the LCDP and $C_{n\beta dyn}$. The research LSR aircraft is in region A in the flight phases of the mission, which indicates no roll departure, as shown in Figure 6(b).

Besides the LCDP and $C_{n\beta dyn}$, the roll–yaw coupling is evaluated as a metric of flight quality. The amplitude ratio of the bank angle over the sideslip angle quantifies the roll reaction to a disturbance in the sideslip angle. An approximation of the roll–yaw coupling can be written as [27]

$$\left|\frac{\phi}{\beta}\right| \approx \left|\frac{\bar{L}_\beta}{\bar{N}_\beta}\right| = \left|\frac{I_{zz}C_{l\beta} + I_{xz}C_{n\beta}}{I_{xz}C_{l\beta} + I_{xx}C_{n\beta}}\right|. \tag{14}$$

The roll–yaw coupling prevents the flying qualities requirements from being satisfied when the flight speed is less than 1.1 Ma [28], having a maximum value of 27 considering the inertia product and 18 without the inertia product, as shown in Figure 7. Without considering the inertia product, Equation (14) can be simplified as

$$\left|\frac{\phi}{\beta}\right| \approx \left|\frac{\bar{L}_\beta}{\bar{N}_\beta}\right| = \left|\frac{C_{l\beta}}{C_{n\beta}}\right| \cdot \frac{I_{zz}}{I_{xx}}. \tag{15}$$

In Equation (15), the roll–yaw coupling is proportional to the value of I_{zz}/I_{xx}, which reflects the slender configuration of the aircraft. Higher values of I_{zz}/I_{xx} indicate worse roll–yaw coupling of the aircraft. As depicted in Figure 7, the roll–yaw coupling value decreases as the Mach number increases. This is because $C_{n\beta}$ and the absolute value of $C_{l\beta}$ decrease, as shown in Figure 3(b). In addition, the negative effect of the inertia product on the roll–yaw coupling weakens as the Mach number increases, allowing the flight quality requirements to be met in the supersonic flight phase. Thus, to avoid roll departure in the subsonic flight phase, the sideslip angle should be suppressed.

2.4. Control Coupling Analysis. During the mission flight phase, the ailerons and rudder are used to control the roll and yaw motions, respectively. However, the control coupling between the ailerons and rudder threatens the flight safety through the undesired moment generated by the deflection in each control channel. As shown in Figure 8, there exists a strong coupling effect between the ailerons and the rudder ($C_{l\delta_a}$ and $C_{n\delta_a}$ are the roll yaw control coefficients of the ailerons, respectively; $C_{l\delta_r}$ and $C_{n\delta_r}$ are the roll and yaw control coefficients of the rudder, respectively).

According to Equation (3), the control matrix for the roll and yaw angular acceleration is

$$B = \begin{bmatrix} \bar{L}_{\delta_a} & \bar{L}_{\delta_r} \\ \bar{N}_{\delta_a} & \bar{N}_{\delta_r} \end{bmatrix}, \tag{16}$$

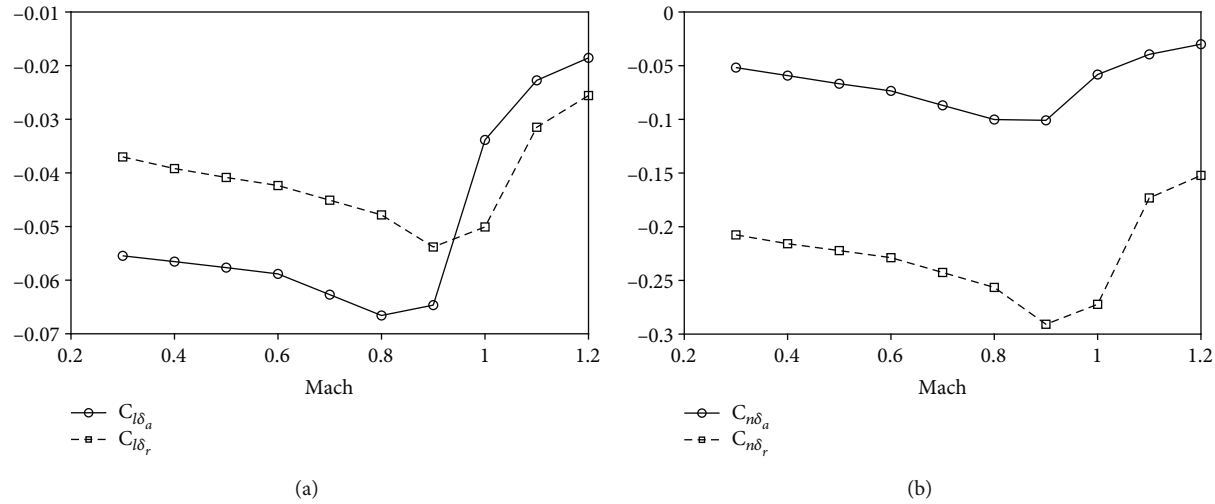

Figure 8: Diagram of roll–yaw control coupling. (a) Roll control coefficients due to the ailerons and rudder deflection (per radian). (b) Yaw control coefficients due to the aileron and rudder deflection (per radian).

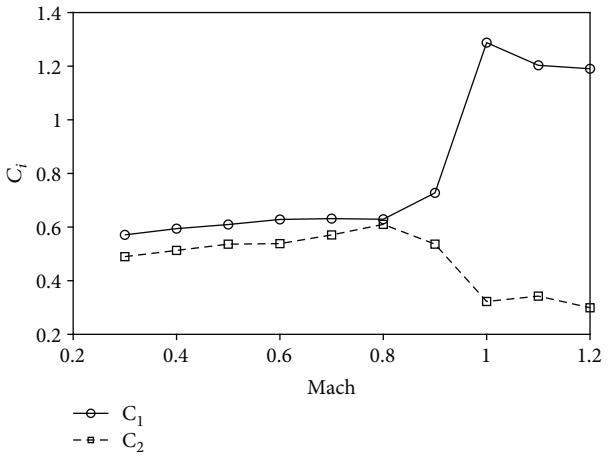

Figure 9: Control-coupling characteristics of the roll and yaw channel (c_1: roll control-coupling parameter; c_2: yaw control-coupling parameter).

where the control effectors are the ailerons and the rudder. The secondary diagonal elements characterize the control coupling of the roll and yaw channels according to

$$c_i = \frac{\sum_{\substack{j=1 \\ j\neq i}}^{m} |b_{ij}|}{|b_{ii}|}, \tag{17}$$

where b_{ij} is the element in the i-th row and j-th column of the control matrix and m is the number of inputs. The parameter c_i characterizes the degree of control coupling—larger values indicate more serious coupling. Consider the parameter c_1 as an example, which represents the control-coupling characteristics of the roll channel.

$$c_1 = \frac{\left|\bar{L}_{\delta_r}\right|}{\left|\bar{L}_{\delta_a}\right|} = \frac{\left|I_{xx}L_{\delta_r} + I_{xz}N_{\delta_r}\right|}{\left|I_{xx}L_{\delta_a} + I_{xz}N_{\delta_a}\right|}, \tag{18}$$

where

$$\begin{aligned} L_{\delta_a} &= \frac{\bar{q}S\bar{b}C_{l\delta_a}}{I_{xx}}, \quad N_{\delta_a} = \frac{\bar{q}S\bar{b}C_{n\delta_a}}{I_{zz}}, \\ L_{\delta_r} &= \frac{\bar{q}S\bar{b}C_{l\delta_r}}{I_{xx}}, \quad N_{\delta_r} = \frac{\bar{q}S\bar{b}C_{n\delta_r}}{I_{zz}}, \end{aligned} \tag{19}$$

in which $\bar{q}$ is the dynamic pressure. Equation (19) can be simplified as

$$c_1 = \frac{\left|C_{l\delta_r} + (I_{xz}/I_{zz})C_{n\delta_r}\right|}{\left|C_{l\delta_a} + (I_{xz}/I_{zz})C_{n\delta_a}\right|}. \tag{20}$$

As shown in Figure 9, the control-coupling characteristics of the roll channel get worse in the transonic flight phase, resulting in considerable control deficiencies. In contrast, the yaw control coupling effect decreases as the Mach number increases. The value of $|C_{\delta_r}/C_{n\delta_a}|$ plays an important role in roll control coupling at small values of I_{xz}/I_{zz}. According to Figure 8(a), the absolute value of $C_{l\delta_r}$ dominates the roll control channel when the Mach number is greater than 0.9, which is undesirable for decoupled control. Therefore, it is difficult for the aircraft to maintain independent roll and yaw manipulation without the coordinated deflection of the control surfaces.

3. Attitude Decoupling Control

Motivated by the above analysis, a lateral–directional decoupling controller for the attitude control of the research LSR aircraft is now designed. The difficulties can be summarized as follows: First, a high roll–yaw coupling characteristic requires the suppression of the sideslip angle during the whole flight mission. Second, the sensitivity of the Dutch-roll mode stability to the inertia product should be taken into consideration, especially in the transonic flight phase. Third, the crossed-coupling between the ailerons and the

rudder should be decoupled. Finally, the model uncertainties and environmental disturbances cannot be ignored. Two kinds of controllers are designed, one based on the MIMO method and the other based on the SISO design. For coordinated flight, the control objectives of the lateral–directional channel are the bank angle and sideslip angle. Considering the lower reliability of the flow-angle measurement unit compared to the inertial measurement unit (IMU), the sideslip angle is substituted for the lateral acceleration.

3.1. MIMO Design Using EA. The EA control method is widely used in the control augmentation system (CAS) design to realize the roll–yaw decoupling control [16]. The output feedback EA is applied here; for the detailed mathematic theory, see reference [29]. First, the state-space model in Equation (3) is rewritten as

$$\begin{bmatrix} \dot{a}_y \\ \dot{p} \\ \dot{r} \\ \dot{\phi} \end{bmatrix} = \underbrace{\begin{bmatrix} \bar{Y}_\beta & (\sin\alpha + \bar{Y}_p)\bar{Y}_\beta U_0 & (\bar{Y}_r - \cos\alpha)\bar{Y}_\beta U_0 & \left(g\cos\frac{\theta}{U_0}\right)\bar{Y}_\beta U_0 \\ \frac{L_\beta}{(\bar{Y}_\beta U_0)} & \bar{L}_p & \bar{L}_r & 0 \\ \frac{\bar{N}_\beta}{(\bar{Y}_\beta U_0)} & \bar{N}_p & \bar{N}_r & 0 \\ 0 & 1 & \tan\theta & 0 \end{bmatrix}}_{A_{lat}} \begin{bmatrix} a_y \\ p \\ r \\ \phi \end{bmatrix} + \underbrace{\begin{bmatrix} \bar{Y}_{\delta_a}(\bar{Y}_\beta U_0) & \bar{Y}_{\delta_r}(\bar{Y}_\beta U_0) \\ \bar{L}_{\delta_a} & 0 \\ 0 & \bar{N}_{\delta_r} \\ 0 & 0 \end{bmatrix}}_{B_{lat}} \begin{bmatrix} \delta_a \\ \delta_r \end{bmatrix}, \tag{21}$$

where U_0 is the trim velocity. Note that the control-coupling parameters $\bar{N}_{\delta_a}$ and $\bar{L}_{\delta_r}$ are disregarded here and will be dealt with in Section 3.3. The modification of the control matrix in Equation (21) separates the control decoupling process from the EA design process, resulting in a more specific target in every design step. To realize tracking control for the lateral acceleration and bank angle, two integrator states are introduced into the augmented lateral–directional coupled model. The extended system matrix and control input matrix are

$$A_{\text{ext}} = \begin{bmatrix} A_{lat} & 0_{4\times 2} \\ -H & 0_{2\times 2} \end{bmatrix} \quad B_{\text{ext}} = \begin{bmatrix} B_{lat} \\ 0_{2\times 2} \end{bmatrix}, \tag{22}$$

where

$$H = \begin{bmatrix} 1 & 0 & 0 & 0 \\ 0 & 0 & 0 & 1 \end{bmatrix}. \tag{23}$$

Because two integrator states are introduced, the output matrix must be extended as

$$C_{\text{ext}} = \begin{bmatrix} I_{4\times 4} & 0_{4\times 2} \\ 0_{2\times 4} & \begin{matrix} 1 & 0 \\ 0 & 1 \end{matrix} \end{bmatrix} \begin{matrix} \cdots e_1, \\ \cdots e_2, \end{matrix} \tag{24}$$

where the states e_1 and e_2 are the integrators of the tracking error for the lateral acceleration and bank angle, respectively. The eigenvalues of the closed loop are the Dutch-roll mode, roll mode, spiral mode, and command tracking integrators. According to the specifications in reference [28], the desired eigenvalues can be chosen to meet the requirement of level 1 flight quality. In addition, the desired eigenvectors V_d of the closed loop should be assigned, as follows:

$$V_d = \begin{matrix} \\ \\ \\ \\ \\ \\ \end{matrix} \begin{matrix} \nu_{DR} & \nu_{DR} & \nu_R & \nu_{SP} & \nu_{e_1} & \nu_{e_2} \end{matrix} \\ \begin{bmatrix} 1 & x & 0 & 0 & x & 0 \\ 0 & 0 & 1 & x & 0 & x \\ x & 1 & 0 & 0 & x & 0 \\ 0 & 0 & x & 1 & 0 & x \\ x & x & 0 & 0 & 1 & 0 \\ 0 & 0 & x & x & 0 & 1 \end{bmatrix} \begin{matrix} a_y \\ p \\ r \\ \phi \\ e_1 \\ e_2 \end{matrix}, \tag{25}$$

where ν_{DR}, ν_R, and ν_{SP} are the desired eigenvectors of the Dutch-roll mode, roll mode, and spiral mode, respectively; ν_{e_1} and ν_{e_2} are the desired eigenvectors of the integrators for the tracking error of the lateral acceleration and bank angle, respectively; and x represents the unrestricted state elements, whereas "0" and "1" denote constrained elements. As shown in Equation (24), the number of outputs is equal to the number of eigenvectors that must be assigned, and so the desired closed-loop eigenvalues can be determined [30]. Furthermore, the tracking speed of the lateral acceleration and bank angle commands depends on the eigenvalues of the integrator modes. Theoretically, the controller can achieve an arbitrary fast rate of error convergence if the poles of the integrators are assigned far away from the imaginary axis in the left-half plane. However, the eigenvalues of the integrators must be chosen according to the control power limit and the rate limit of the effectors. Following reference [16], the stabilization feedback gain K and the command tracking gain L can be obtained. The control diagram of the lateral–directional decoupling controller is shown in Figure 10, in which the parameters ϕ_c and a_{yc} are the bank angle and lateral acceleration command values, respectively.

3.2. SISO Design Using ESO. Another control method based on the SISO design method is established to realize decoupled control for the lateral–directional dynamics of the research LSR aircraft. This controller divides the lateral–directional motion of the aircraft into fast-speed inner loops and low-speed outer loops and then uses the time-scale-separation principle to realize attitude control. First,

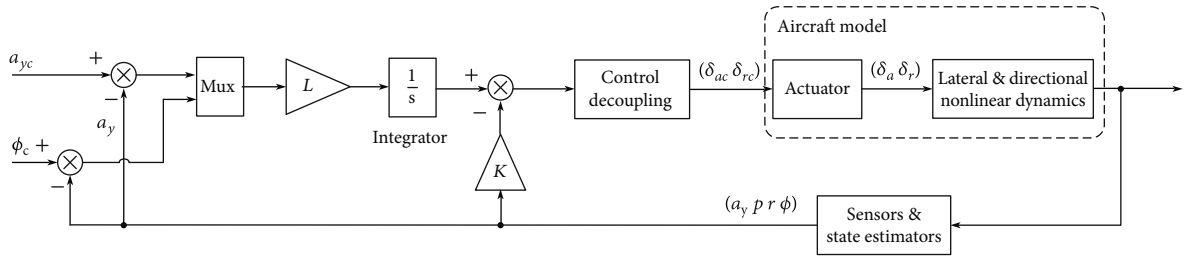

Figure 10: Lateral–directional EA control loop.

the lateral acceleration and bank angle commands are given to the outer loops, which generate the yaw and roll angular rate commands for the inner loops. Second, the inner loops realize precise angular rate tracking commands using the rudder and ailerons.

For the angular rate control loops, the equations of the dynamics can be written as

$$\begin{aligned} \dot{p} &= f_p + L_{\delta_a}\delta_a, \\ \dot{r} &= f_r + N_{\delta_r}\delta_r, \end{aligned} \tag{26}$$

where f_p and f_r are the lumped disturbance of the roll and yaw angular rate control loops, including the internal coupling dynamics, model uncertainties, and environmental disturbances. In addition, the derivatives of f_p and f_r are assumed to be unknown but bounded [31], as in the following equation:

$$\begin{aligned} f_p &= \frac{(I_{yy}-I_{zz})I_{zz}-I_{xz}^2}{I_{xx}I_{zz}-I_{xz}^2}rq + \frac{(I_{xx}-I_{yy}+I_{zz})I_{xz}}{I_{xx}I_{zz}-I_{xz}^2}pq \\ &\quad + \frac{I_{zz}}{I_{xx}I_{zz}-I_{xz}^2}L + \frac{I_{xz}}{I_{xx}I_{zz}-I_{xz}^2}N - L_{\delta_a}\delta_a, \\ f_r &= \frac{(I_{xx}-I_{yy})I_x+I_{xz}^2}{I_{xx}I_{zz}-I_{xz}^2}pq - \frac{(I_{xx}-I_{yy}+I_{zz})I_{xz}}{I_{xx}I_{zz}-I_{xz}^2}qr \\ &\quad + \frac{I_{xx}}{I_{xx}I_{zz}-I_{xz}^2}N + \frac{I_{xz}}{I_{xx}I_{zz}-I_{xz}^2}L - N_{\delta_r}\delta_r, \end{aligned} \tag{27}$$

where L and N are the roll and yaw moments imposed on the aircraft, respectively, which are composed of the moments induced by the aerodynamic effectors and wind disturbance. In the ESO-based controller, the inner-loop coupling dynamics are regarded as the disturbance that must be estimated and then compensated in real time. For simplicity, the original nonlinear ESO is replaced with a linear form that simplifies the adjustment of the control parameters [32]. However, the nonlinear ESO has some advantages in terms of low peaking levels and more accurate estimation [33]. A second-order nonlinear ESO is used in the angular rate control loop:

$$\begin{aligned} e_1 &= z_1 - y, \\ \dot{z}_1 &= z_2 + b_0 u - \beta_1 e_1, \\ \dot{z}_2 &= -\beta_2 fal(e_1, \alpha, \delta), \end{aligned} \tag{28}$$

where z_1 and z_2 are the estimations of the angular rate and lumped disturbance for each control channel, respectively; y is the measurement value of the angular rate; b_0 is the parameter related to the control efficiency; and β_1 and β_2 are the ESO parameters, which need to be tuned carefully. The nonlinear function fal is defined as

$$fal(e_1, \alpha, \delta) = \begin{cases} \dfrac{e_1}{\delta^{1-\alpha}}, & |e_1| \le \delta, \\ |e_1|^{\alpha}\ \text{sign}\ (e_1), & |e_1| > \delta, \end{cases} \tag{29}$$

where $0 < \alpha < 1$ and $\delta > 0$ are the observer parameters, and the sign function is defined as

$$\text{sign}\ (x) = \begin{cases} 1, & x > 0, \\ 0, & x = 0, \\ -1, & x < 0. \end{cases} \tag{30}$$

The control law of the angular rate control loop is

$$u = \frac{u_0 - z_2}{b_0}, \tag{31}$$

where u_0 is the output of the proportional controller, given by

$$u_0 = k(\omega_c - \omega), \tag{32}$$

where $\omega_c \in [p_c, r_c]$ denotes the roll and yaw angular rate command values; $\omega \in [p, r]$ denotes the roll and yaw angular rate measured values; $k \in [k_p, k_r]$ represents the gains of the proportional controller, where k_p and k_r are the closed-loop control bandwidths of the roll and yaw channels, respectively. According to Equation (31), the original system in Equation (26) can be converted to a pure integrator system under the assumption that the lumped disturbance is accurately estimated using ESO. As a result, the closed loop of

the angular rate control can be regarded as a first-order transfer function:

$$\frac{\omega(s)}{\omega_c(s)} = \frac{k}{s+k}. \tag{33}$$

For the stability analysis of the ESO-based controller, Guo et al. first gave the convergence analysis for the nonlinear systems with uncertainty [34]. The system in Equation (26) can be rewritten as

$$\begin{aligned} \dot{x}_1 &= x_2 + b_0 u, \\ \dot{x}_2 &= w, \end{aligned} \tag{34}$$

where x_1 is the state variable; x_2 is the lumped disturbance, unknown but bounded and continuously differentiable is assumed; and w is the derivative of the lumped disturbance which satisfies $|w| < w_H$ according to Equation (27). Combing the second-order nonlinear ESO in Equation (28), the equations of estimation error can be constructed as

$$\begin{aligned} e_2 &= z_2 - x_2, \\ \dot{e}_1 &= e_2 - \beta_1 e_1, \\ \dot{e}_2 &= -\beta_2 fal(e_1, \alpha, \delta) - w. \end{aligned} \tag{35}$$

According to reference [35], the estimation errors e_1 and e_2 are bounded when the observer gain β_1 and β_2 are adjusted properly. If the parameter α is equal to one, the function fal becomes a linear form, and the error bound becomes $|w|/\beta_2$. However, the error bound becomes $(|w|/\beta_2)^2$ using the nonlinear form in Equation (29) which shows the efficiency of the nonlinear ESO, and the value of β_2 needs to be bigger than w_H.

For the outer-loop bank angle control, NDI is used. The kinematic relationship between the bank angle and roll angular rate is given by Equation (2). The bank angle rate is replaced by a virtual control v_ϕ, which is defined as

$$v_\phi = k_\phi(\phi_c - \phi), \tag{36}$$

where the parameter k_ϕ is the closed-loop control bandwidth of the bank angle. Furthermore, the roll angular rate command value can be derived as

$$p_c = v_\phi - \tan\theta(q\sin\phi + r\cos\phi). \tag{37}$$

According to Equation (3), the transfer function from the yaw angular rate to the sideslip angle can be obtained without considering gravity, inertial coupling, or damping effects, as shown in the following equation.

$$\frac{\beta(s)}{r(s)} = -\frac{1}{s + Y_\beta}, \tag{38}$$

where

$$Y_\beta = \frac{\bar{q}SC_{Y\beta}}{mV}, \tag{39}$$

in which $C_{Y\beta} < 0$ is the side force coefficient induced by the sideslip angle. The relationship between the lateral acceleration and the sideslip angle can be written as

$$a_y = Y_\beta V\beta. \tag{40}$$

According to Equation (33), the inner closed loop can be simplified as a first-order inertia element, and a proportional–integral (PI) compensator is used for tracking control of the lateral acceleration, as depicted in Figure 11.

With PI compensation, the closed transfer function for the lateral acceleration command to the measured output is a second-order nominal model that can be expressed as

$$\frac{a_y(s)}{a_{yc}(s)} = \frac{k_a k_r}{s^2 + k_r s + k_a k_r}. \tag{41}$$

The damping ratio is selected as 0.8, and the controller gain k_a is calculated as

$$k_a = \frac{k_r}{1.6^2}. \tag{42}$$

In addition, the yaw angular rate command is compensated using the maneuvering turn angular rate for coordinate flight, given by

$$\begin{aligned} \Omega_c &= g\tan\phi/V_g, \\ r_{co} &= \Omega_c\cos\phi\cos\theta, \end{aligned} \tag{43}$$

where Ω_c is the maneuvering turn rate, V_g is the ground velocity, and r_{co} is the compensated yaw angular rate command value. The overall control structure of the lateral–directional decoupling control based on ESO is shown in Figure 12.

3.3. Hard Cross-Connection. According to the control-coupling analysis in Section 2.4, there exists a strong coupling between the roll and yaw control effectors. To overcome the control coupling between the ailerons and rudder, a hard cross-connection method [16] is applied. Both the aileron–rudder interconnect (ARI) and the rudder–aileron interconnect (RAI) are used here [36], whereby the command deflection angle of one channel is fed directly into the other.

The control matrix of the roll and yaw angular acceleration is presented in Equation (16). The desired decoupled control matrix is

$$B_{des} = \begin{bmatrix} \bar{L}_{\delta_a} & 0 \\ 0 & \bar{N}_{\delta_r} \end{bmatrix}. \tag{44}$$

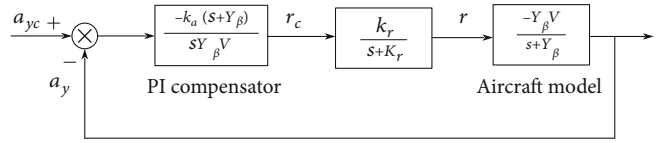

Figure 11: Diagram of the lateral acceleration control.

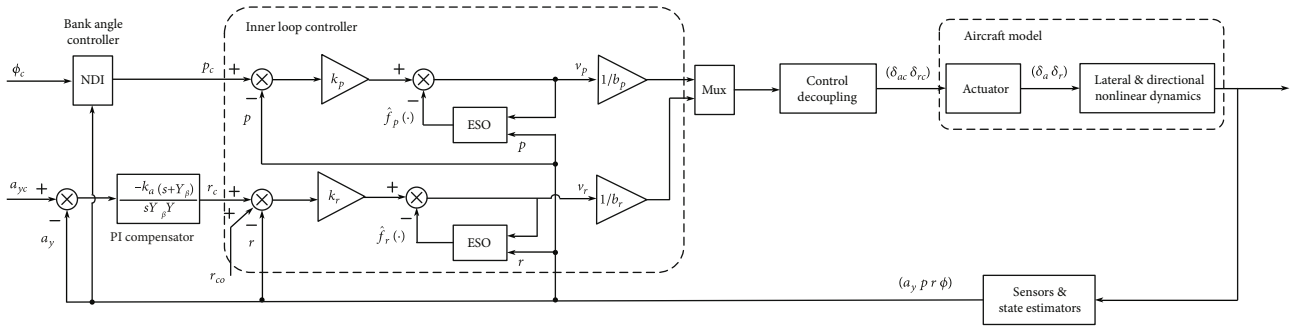

Figure 12: Lateral–directional ESO-based control loop.

Table 4: Characteristics of the control effectors.

Actuator	Rate limit (deg/s)	Position limit (deg)	Damping ratio	Natural frequency (rad/s)
Aileron, δ_a	±120	±25	0.7	60
Rudder, δ_r	±120	±20	0.7	60

Table 5: Eigenvalues and eigenvectors for the open-loop lateral-directional dynamics.

Eigenvalues	Dutch roll	$-0.244 \pm j4.83$		
	Roll	-2.45		
	Spiral	-0.0238		
Eigenvectors	a_y	$0.8210 \pm j0$	0.0127	-0.0350
	p	$0.2423 \pm j0.5018$	-0.9260	-0.0249
	r	$0.0025 \pm j0.0465$	-0.0097	0.0401
	ϕ	$-0.1059 \pm j0.0449$	0.3773	0.9983

In Equation (44), the off-diagonal elements are zero, which means the roll and yaw channel are decoupled. The hard cross-connection matrix $K_{hc} \in R^{2\times 2}$ is defined here, and the linear control allocation problem with equality constrained expressed as

$$BK_{hc} = B_{des}. \tag{45}$$

Clearly, the control matrix B is square and invertible [37]. Thus, the pseudoinverse method is applied to realize control decoupling as

$$K_{hc} = B^{\dagger}B_{ep}, \tag{46}$$

Table 6: Desired eigenvalues of the closed loop.

Name	Eigenvalue
Dutch-roll mode λ_{DR}	$-4.0\text{s} \pm j3.0$
Roll mode λ_R	-8.0
Spiral mode λ_{sp}	-6.0
Lateral acceleration error integral mode λ_{e_1}	-2.0
Bank angle error integral mode λ_{e_2}	-2.0

where $B^{\dagger} = B^T(BB^T)^{-1}$ is the pseudoinverse of the control matrix. The saturation of the control surfaces is ignored due to the requirement for the deflection angle to be quite small because of the high dynamic pressure over the whole flight regime. Additionally, under significant changes of the control matrix during flight, the hard cross-connection decoupling matrix K_{hc} should be scheduled according to the Mach number.

4. Simulation Results

4.1. Linear Analysis and Simulation of the EA-Based Control. The research LSR aircraft is trimmed at a speed of Mach 0.8 and an altitude of 10,000 m. The effectors are modeled as a second-order dynamic system with position and rate limitations, as summarized in Table 4.

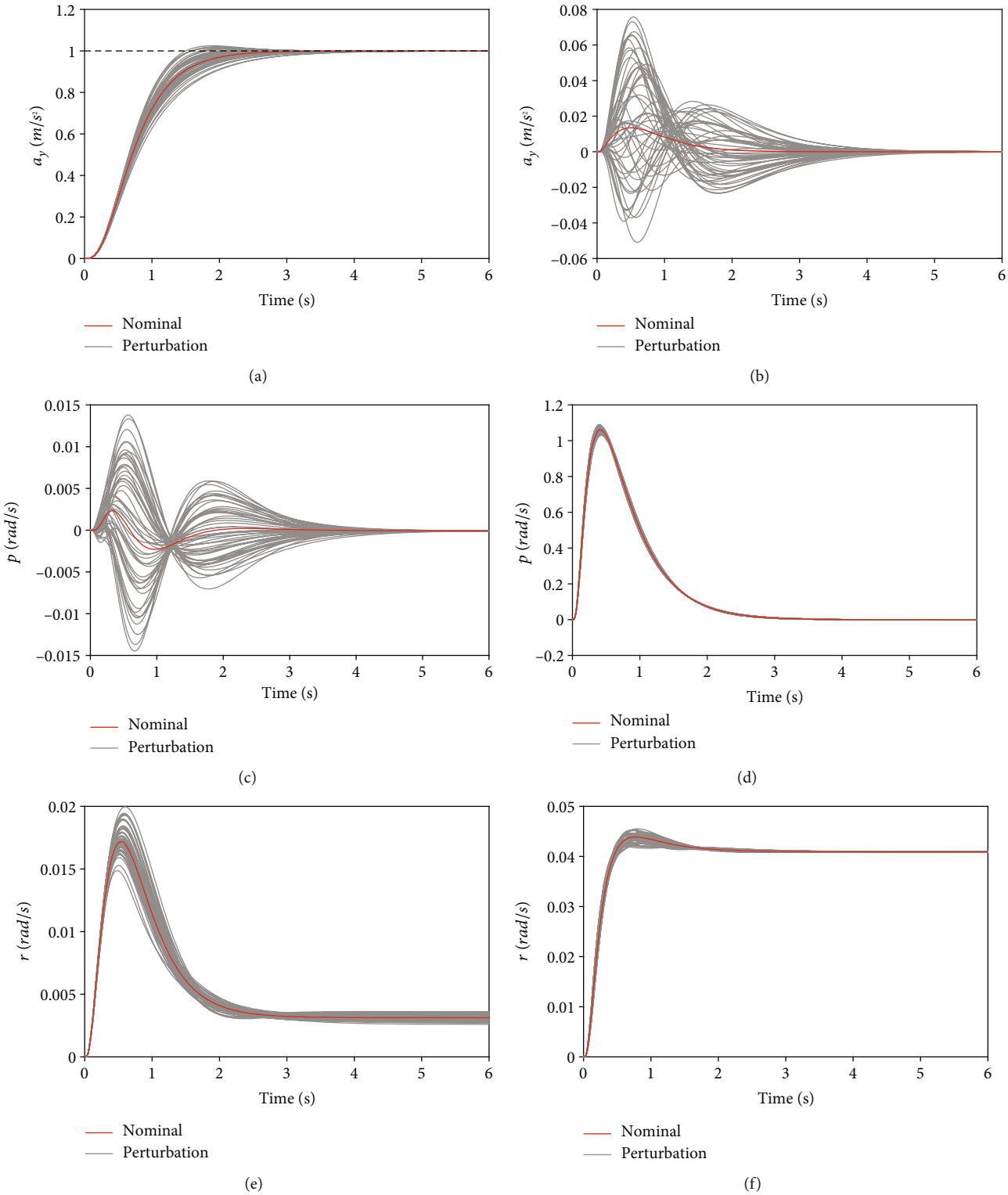

Figure 13: Continued.

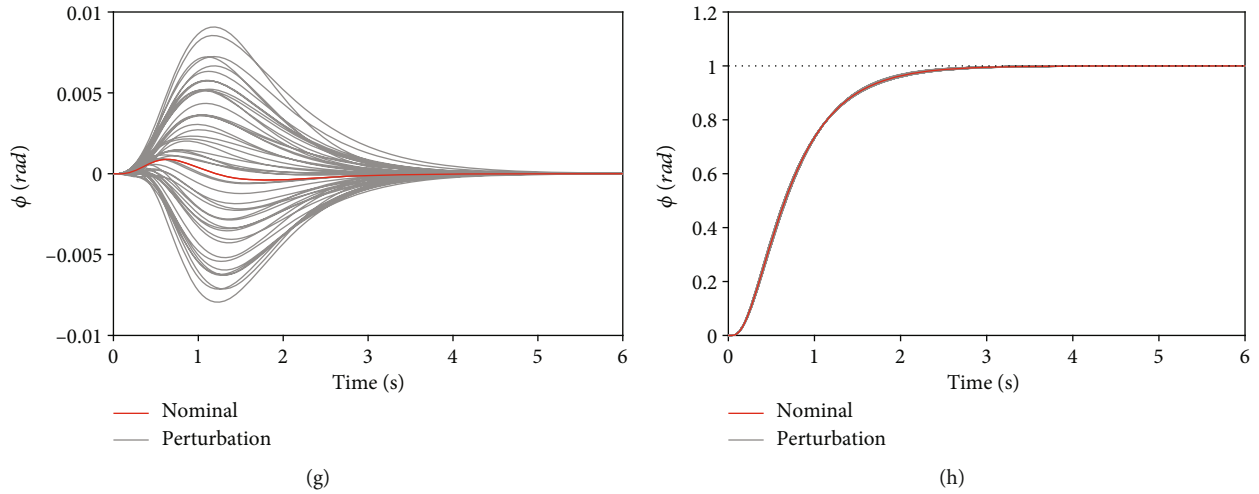

Figure 13: Step response of the closed loop with EA control. (a) a_{yc} to a_y response. (b) ϕ_c to a_y response. (c) a_{yc} to p response. (d) ϕ_c to p response. (e) a_{yc} to r response. (f) ϕ_c to r response. (g) a_{yc} to ϕ response. (h) ϕ_c to ϕ response.

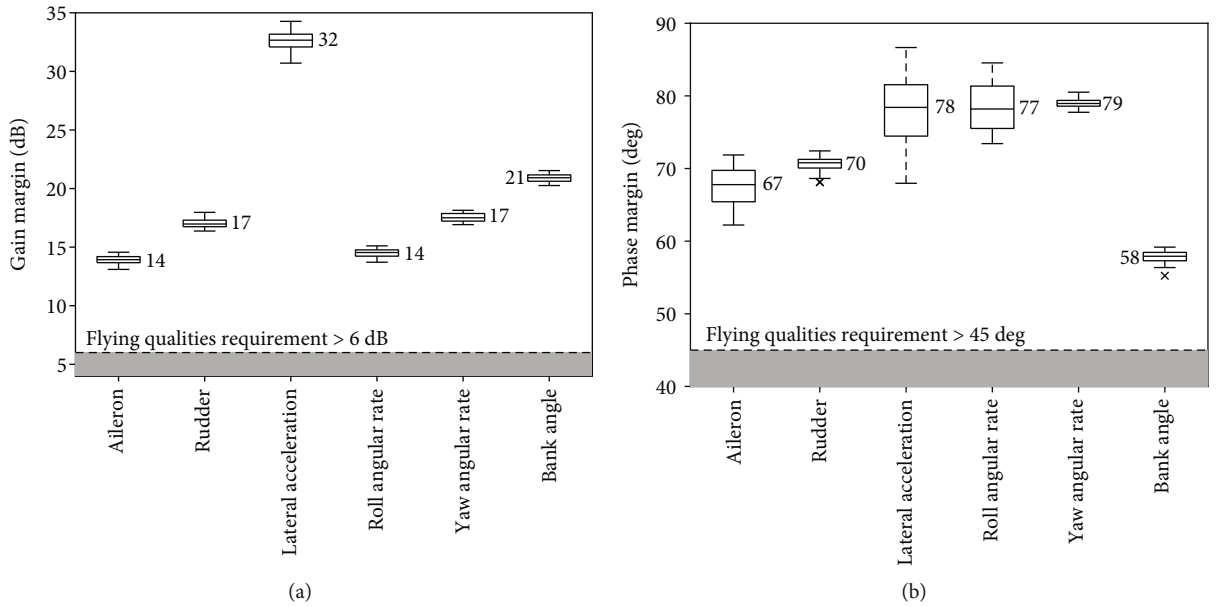

Figure 14: Phase margin and gain margin (median values are shown). (a) Gain margin at the breakpoints of the input and output. (b) Phase margin at the breakpoints of the input and output.

Table 7: ESO and outer loop control parameters.

Parameter	Explanation	Value
k_ϕ	Bank angle control gain	1.5
k_p	Roll angular rate control bandwidth	10
β_{1p}	Roll angular rate ESO gain	10
β_{2p}	Roll angular rate ESO gain	8
α	ESO *fal* function parameter	0.5
δ	ESO *fal* function parameter	0.01
k_a	Lateral acceleration control gain	1.95
k_r	Yaw angular rate control bandwidth	5
β_{1r}	Yaw angular rate ESO gain	10
β_{2r}	Yaw angular rate ESO gain	8

First, for the MIMO control law based on EA, the nonlinear model is linearized at the trimmed point, and the state variables are a_y, p, r, and ϕ. The open-loop lateral–directional eigenvalues and eigenvectors are listed in Table 5. The real parts of the eigenvalues are all negative, implying that the lateral–directional modes are all stable. However, the damping ratio of the Dutch-roll mode is only 0.05, which does not satisfy the military specifications. The minimum damping ratio and natural frequency for level 1, category A, class IV flight vehicles [38] are 0.4 and 1 rad/s, respectively. Furthermore, the eigenvectors of the roll and yaw channels are coupled.

To realize decoupling control and satisfy the flight quality requirements, the desired eigenvalues are as listed in

Table 8: Parameter uncertainties in the nonlinear simulations.

Parameter	Explanation	Uncertainty (%)
I_{xz}, I_{xx}, I_{zz}, m	Inertial parameters	±20
$C_{l\delta_a}$, $C_{n\delta_r}$	Control coefficients	±30
$C_{Y\beta}$, $C_{Y\delta_r}$, $C_{l\beta}$, $C_{n\beta}$	Static aero coefficients	±20
$C_{l\delta_r}$, $C_{n\delta_a}$	Control coupling coefficients	±20
C_{Yp}, C_{Yr}	Aero coefficients of damping force	±50
C_{lr}, C_{np}, C_{lp}, C_{nr}	Aero coefficients of damping moment	±80
$\bar{q}$, $\bar{a}$	Dynamic pressure and airspeed	±15

Table 6. The desired damping ratio and natural frequency for the Dutch-roll mode are 0.8 and 5 rad/s, respectively. In addition, the closed-loop spiral mode is set to -6 here. This is in sharp contrast to the conventional conception that the spiral mode should be close to zero. To avoid the coupling effect of the dominant poles of the error integral modes, the closed-loop spiral mode should be placed far away from the integral modes.

The feedback gain K and the command tracking gain L can be obtained through EA calculations:

$$L = \begin{bmatrix} 0.0003 & -0.6737 \\ -0.0534 & -0.1777 \end{bmatrix},$$
$$K = \begin{bmatrix} -0.0250 & -0.0953 & -0.0117 & -0.5334 \\ -0.0232 & -0.0069 & -0.6440 & -0.1128 \end{bmatrix}. \quad (47)$$

The MATLAB control toolbox [39] is used to compute the linear response and stability margins for the parameter uncertainties. The uncertainties of the stability derivatives are $\bar{Y}_\beta = 10\%$, $\bar{Y}_p = 10\%$, $\bar{Y}_r = 10\%$, $\bar{L}_\beta = 30\%$, $\bar{L}_p = 50\%$, $\bar{L}_r = 50\%$, $\bar{N}_\beta = 30\%$, $\bar{N}_p = 50\%$, and $\bar{N}_r = 50\%$. The control uncertainties are 15% for all control derivatives. A step command value is supplied to the linear closed-loop system by the actuator model, and the responses are shown in Figure 13.

As shown in Figure 13, the requirements for precise tracking control and lateral–directional decoupling control are achieved under model uncertainties. Furthermore, the time constants of the lateral-acceleration and bank-angle tracking control are about 0.3 and 0.5, respectively. These time constants are consistent with the assigned eigenvalues. To further evaluate the frequency characteristics of the controller, the phase margin and gain margin at the breakpoints of the control input and model output are depicted in Figure 14. In Figure 14(a), the gain margins with the actuator model are all greater than 6 dB, while the phase margins are greater than 45 degrees in Figure 14(b), satisfying the specifications of 6 dB and 45 deg. In addition, the margins remain within the specifications under parameter perturbations, demonstrating the robustness of the controller.

4.2. Nonlinear Simulation of the ESO-Based Control. First, the control effectiveness parameter b_0 in Equation (28) is selected as

$$b_p = L_{\delta_a} = \frac{\bar{q}SbC_{l_{\delta_a}}}{I_{xx}},$$
$$b_r = N_{\delta_r} = \frac{\bar{q}SbC_{n_{\delta_r}}}{I_{zz}}, \quad (48)$$

where b_p and b_r are the parameters of the roll and yaw control channels, respectively. The control coefficients of the roll moment $C_{l\delta_a}$ and yaw moment $C_{n\delta_r}$ are scheduled according to the Mach number over the whole flight regime based on a reliable CFD calculation. The left parameters of the ESO and outer-loop controllers are listed in Table 7. According to reference [31], the gains of β_1 and β_2 in the ESO controller can be approximately as

$$\beta_1 = 2\omega_o,$$
$$\beta_2 = \frac{\omega_o^2}{3}, \quad (49)$$

where ω_o can be adjusted using the bandwidth method [32]. By trial and error, the bandwidths of the observers are chosen as 5 rad/s for both the roll and yaw control channels. The absolute stability convergence analysis is given in reference [40].

Second, to verify the tracking performance and robustness of the ESO-based controller, Monte Carlo simulations are conducted using the nonlinear model with the actuator model. The simulations are initialized using the trim condition in Section 4.1. For longitudinal control, the flying altitude and speed are maintained. The uncertainties of the inertial parameters and aerodynamic parameters are listed in Table 8.

Latin hypercube sampling [41] is used in the MC simulations to improve the degree of coverage with fewer sampling events. A doublet bank angle command is given to

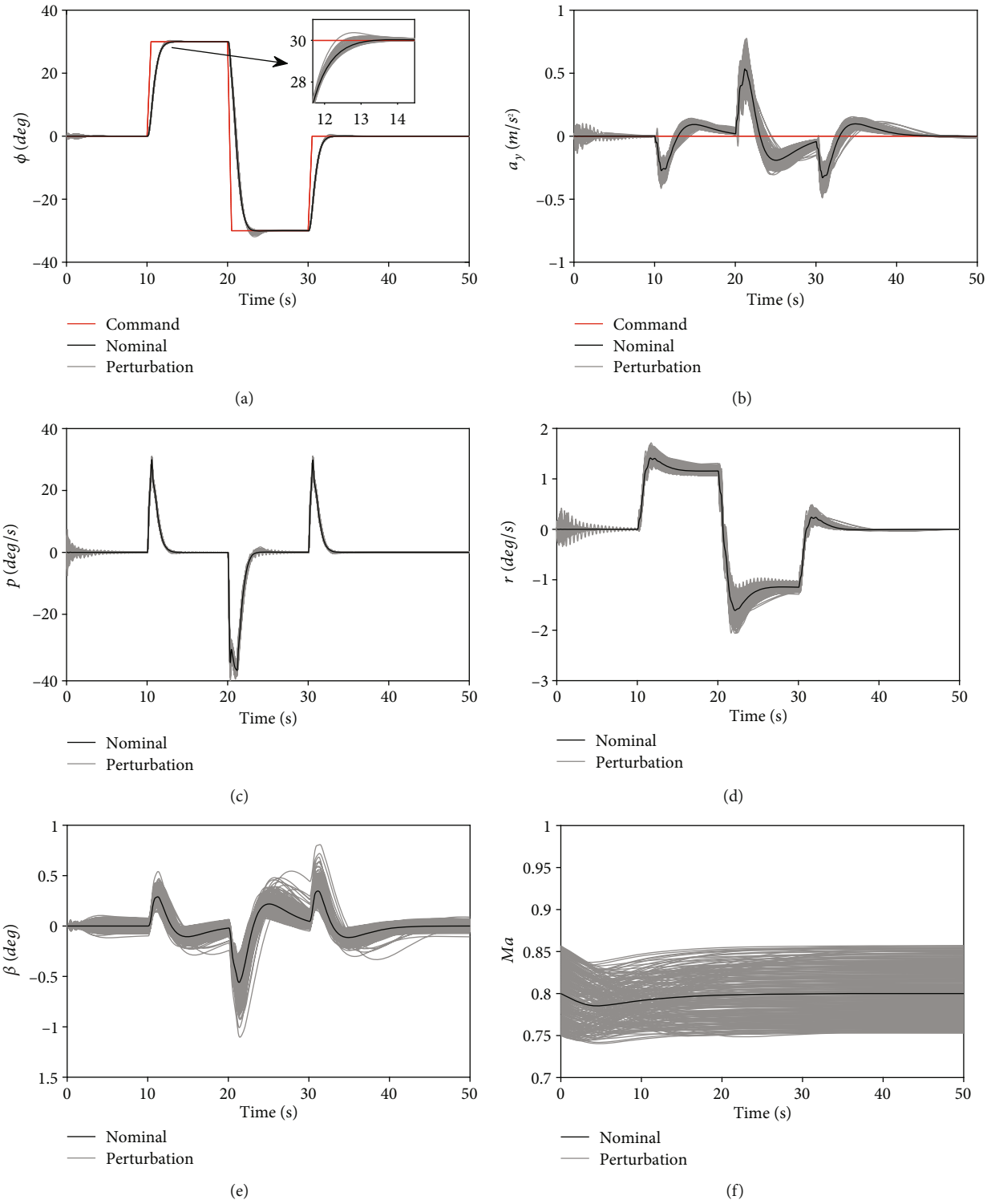

Figure 15: Continued.

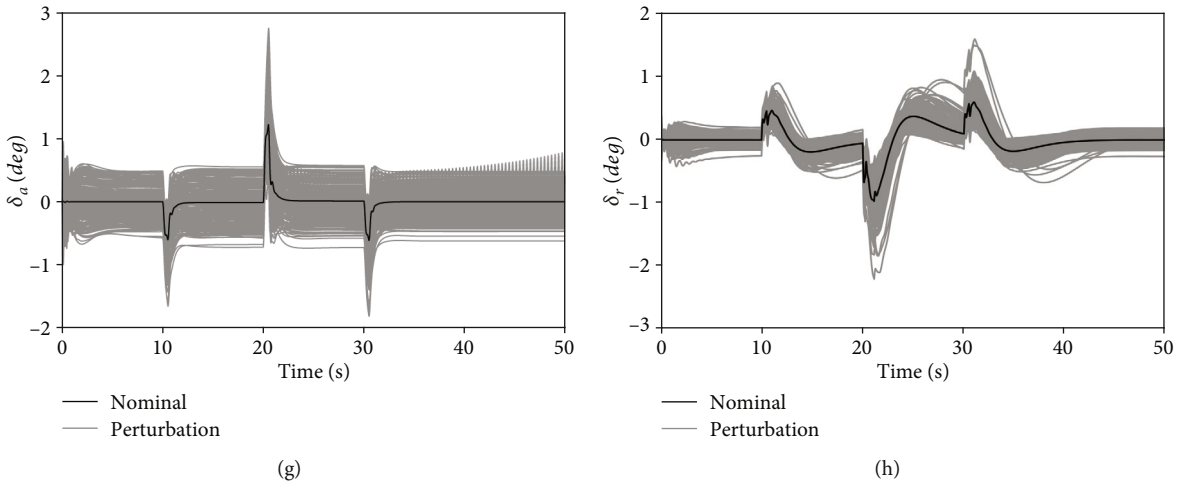

Figure 15: Results of MC simulations of the ESO-based control. (a) Bank angle response. (b) Lateral acceleration response. (c) Roll angular rate response. (d) Yaw angular rate response. (e) Sideslip angle response. (f) Velocity response. (g) Aileron command value. (h) Rudder command value.

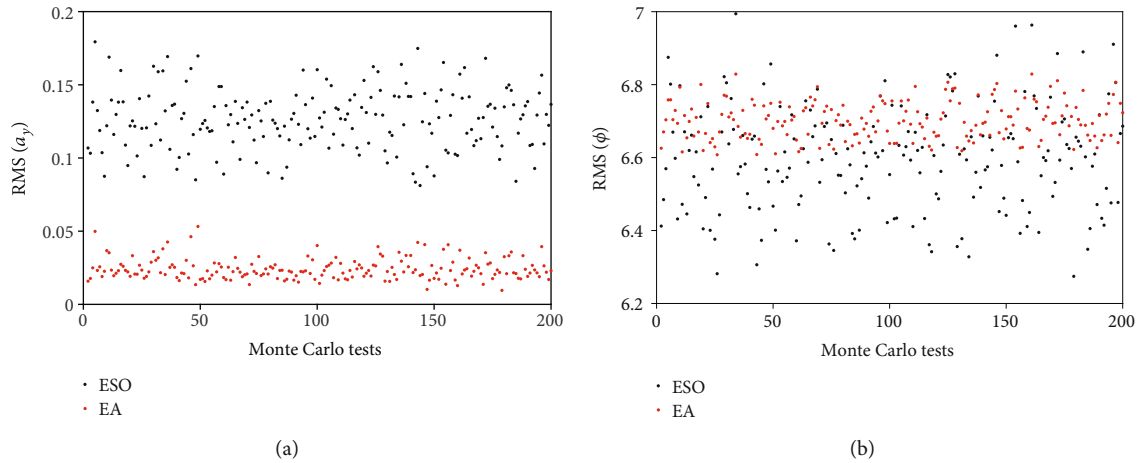

Figure 16: Comparison of MC simulations. (a) RMS of the lateral acceleration control. (b) RMS of the bank angle control.

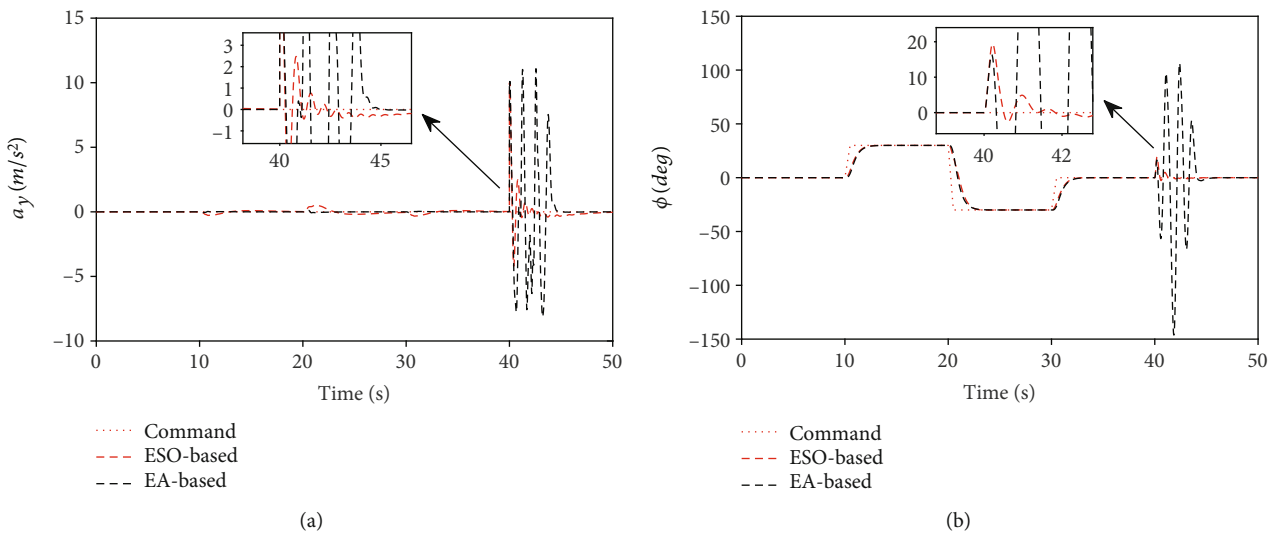

Figure 17: Simulation results with wind disturbance. (a) Lateral acceleration response. (b) Bank angle response.

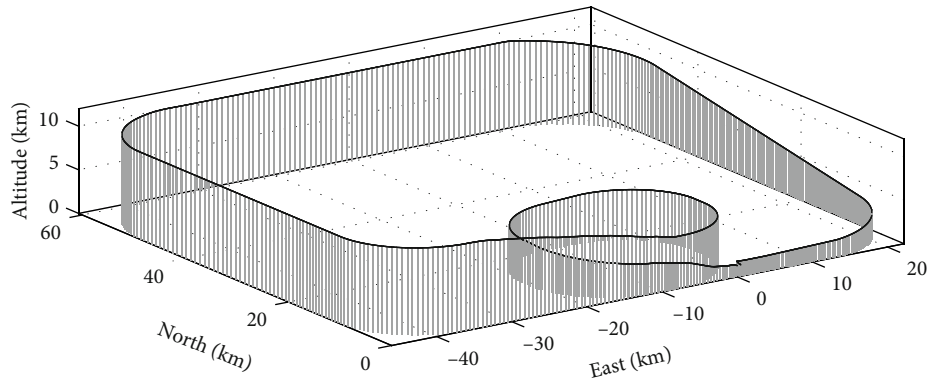

Figure 18: Flight trajectory of the mission.

the system while the acceleration command is set to zero. Furthermore, 200 MC simulations are conducted. The simulation results are shown in Figure 15.

As shown in Figure 15(f), the aircraft enters the transonic flight regime due to airspeed uncertainties. The transonic flight regime leads to a significant change in aerodynamic performance which poses a great threat to the control quality. In Figures 15(e) and 15(a), the maximum value of $|\beta/\phi|$ is about 0.033, resulting in decoupled control of the roll and yaw channels. The maximum deflection angles of the ailerons and rudder are 2.8 and 2.1 degrees, respectively, as a result of high dynamic pressure, as shown in Figures 15(g) and 15(h). Precise tracking performance of the bank angle is achieved without overshoot, as depicted in Figure 15(a). The rising time of the bank angle control is about 0.67 s and remains consistent under model parameter perturbations, which demonstrates the robustness of the ESO-based controller.

4.3. Comparison of Control Performance. First, the model uncertainties listed in Table 8 are applied to the nonlinear model for MC simulations using ESO-based and EA-based attitude control. To quantify the attitude tracking performance, the RMS of the tracking error is evaluated:

$$\mathrm{RMS}(x) = \sqrt{\frac{1}{N}\sum_{n=1}^{N} |x_c(t) - x(t)|^2}, \tag{50}$$

where $x(t)$ and $x_c(t)$ are the state response and command value, respectively, and N is the number of MC simulations. The RMS calculation results of the two controllers are shown in Figure 16. Figure 16(a) gives the RMS of the lateral acceleration control, where the EA-based control exhibits better performance than the ESO-based control. However, in Figure 16(b), the ESO-based control has a slight advantage in the RMS value for the bank angle tracking control. The conclusion is that the EA-based controller achieves better decoupling characteristics for the lateral–directional dynamics resulting from the MIMO design method. Furthermore, the SISO design method means that the ESO-based controller struggles to completely compensate for the residual coupling nonlinearities.

Second, to further evaluate the disturbance rejection characteristics of the two controllers, discrete gusts of wind are taken into consideration. The discrete gusts have a "1-cosine" shape given by [28]

$$V_{\text{wind}} = \begin{cases} 0, & x_d < 0, \\ \dfrac{V_m}{2}\left(1 - \cos\left(\dfrac{\pi x_d}{d_m}\right)\right), & 0 \le x_d \le d_m, \\ V_m, & x_d > d_m, \end{cases} \tag{51}$$

where V_m is the gust amplitude, d_m is the gust length, x_d is the distance travelled, and V_{wind} is the resultant wind velocity. The gust length $d_m = 120$ m and the gust amplitude $V_m = 20$ m/s are chosen according to the specifications in [28]. To evaluate the control performance under the most extreme scenario, another step gust wind with an amplitude of 10 m/s is added to the 1-cosine wind gust model. The wind gust occurs after 40 s, as shown in Figure 17. The tracking performance of the bank angle is almost the same for the two controllers without the wind gusts, as shown in Figure 17(b). When wind gusts occur, the EA-based controller produces sharp oscillations in both the roll and yaw channels. In addition, the oscillations last 5 s. Under parameter perturbations, this oscillation may easily activate roll–yaw coupling, whereby the aircraft loses control. Contrary to the EA-based controller, the ESO-based controller enables rapid convergence of the tracking error, with a convergence period of less than 1.5 s and little oscillation. Thus, the ESO-based attitude controller has better disturbance rejection performance.

5. Flight Test Validation

Considering the complexity of tuning the parameters of the EA-based control and the risk associated with discontinuities while switching the control parameters due to gain scheduling, the SISO ESO-based control was chosen as the flight test control law. A large number of MC simulations

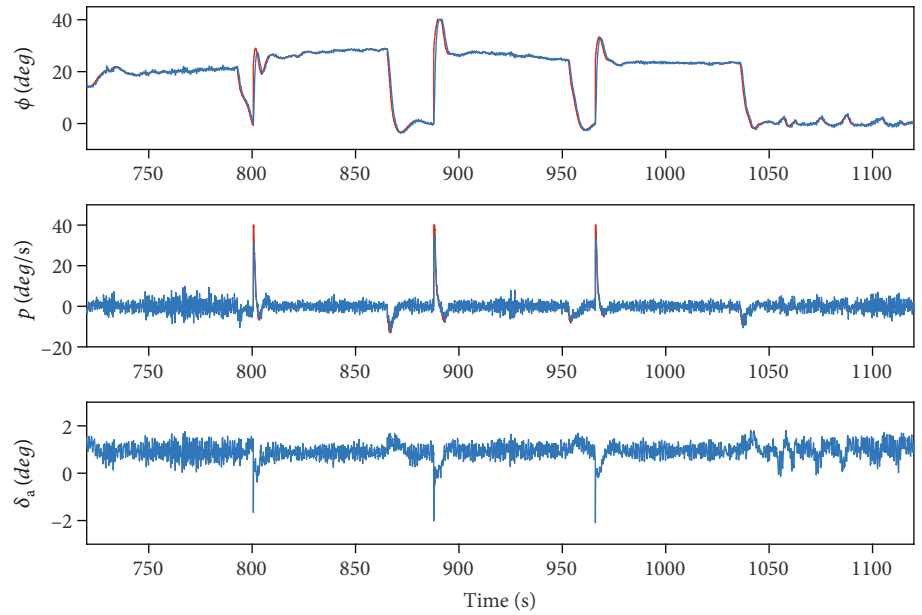

(a)

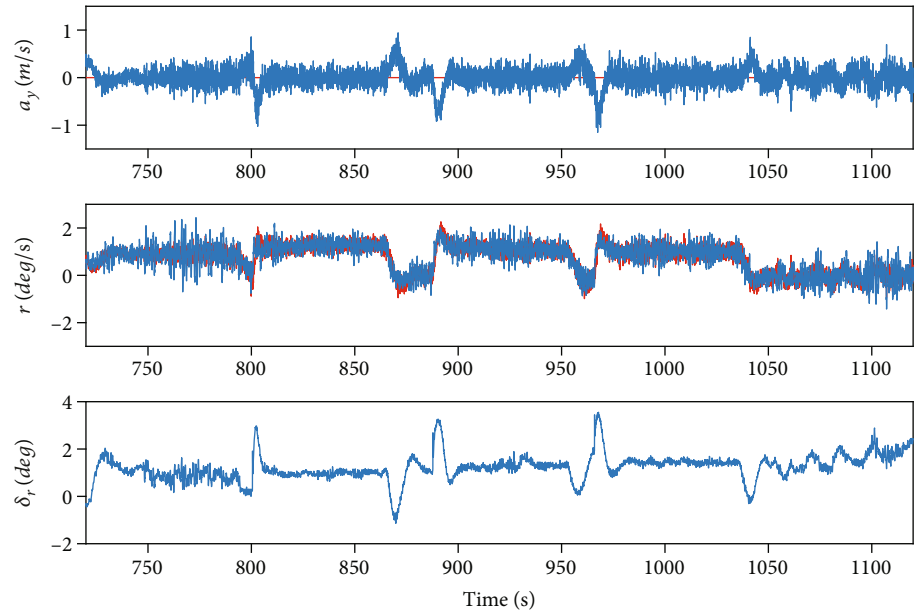

(b)

Figure 19: Continued.

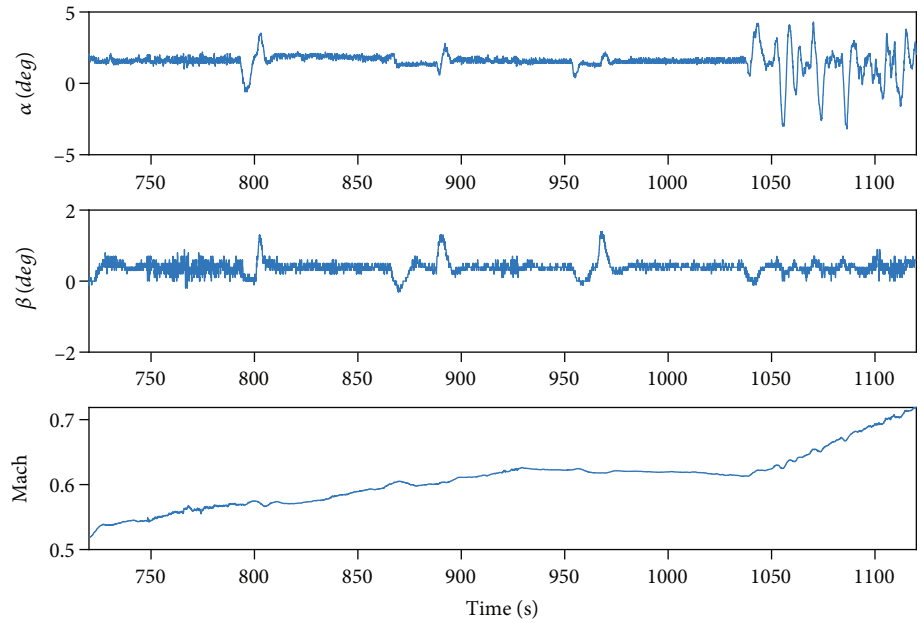

(c)

Figure 19: Flight test data. (a) Command and response value of the roll channel. (b) Command and response values of the yaw channel. (c) Response of other states.

Table 9: RMS of the tracking error for flight test and simulation.

Parameter	a_y (m/s^2)	r (deg/s)	p (deg/s)	ϕ (deg)
RMS of flight	0.21	0.39	2.26	1.81
RMS of HIL simulation	0.13	0.15	3.29	1.69

were conducted before the flight to ensure flight safety. In addition, detailed emergency measures were proposed to avoid various flight risks. Hardware-in-the-loop (HIL) simulations were compared with software-in-the-loop (SIL) results, and the sample time of the autopilot was set to 5 ms. An extended Kalman filter was used to estimate the attitude angles and angular rates in the flight test, and the airflow angles were measured using a wind vane at the nose position, as shown in Figure 1. During the flight mission, the parameters of the ESO were fixed, except for the effectiveness-related parameter b_0, which was scheduled according to the Mach number. Thus, the ESO-based attitude controller was used in the entire flight mission with a simple SISO design method and without the need to tune various control parameters. Figure 18 shows the three-dimensional flight trajectory of the mission.

The attitude tracking performance of the ESO-based controller is shown in Figure 19. During the flight test, lateral–directional decoupling control was achieved. Table 9 compares the RMS values between the flight test and HIL simulations. The flight test values are consistently close to the HIL simulation. Therefore, the simulations provide reliable results because of the high-fidelity dynamics model and the realistic simulation environment.

As depicted in Figure 19(a), the bank angle was tracked without any steady errors or overshoot, illustrating the precise tracking performance of the roll angular rate. This is consistent with the simulation results shown in Section 4.3. In addition, the maximum value of the ailerons is about 2 degrees, which is close to the simulation results in Figure 15(g). The angle-of-attack is less than 4 degrees over the whole flight, satisfying the small angle-of-attack assumption in Equation (9), as shown in Figure 19(c). In Figure 19(b), the lateral acceleration is less than 1 m/s^2 during the flight, and the yaw angular rate exhibits good command tracking performance. According to Figures 19(b) and 19(c), the maximum value of $|\beta/\phi|$ is about 0.045, which is slightly higher than the simulation results shown in Section 4.2.

6. Conclusions and Further Work

For the lateral–directional coupling dynamics analysis and control of an LSR supersonic aircraft, this study has elicited the following research results:

(1) The inertia product plays an important role in the coupling dynamics of the LSR aircraft and cannot be ignored in the design process. In addition, the stability of the Dutch-roll mode is most sensitive to the value of the inertia product during the transonic phase. Additional wingtip weights should be considered when there is a risk of instability

(2) Roll–yaw coupling poses a great threat to flight safety in the case of LSR aircraft. As the angle-of-attack increases, the value of roll–yaw coupling increases sharply. Therefore, the attitude controller

of the LSR aircraft must suppress the sideslip angle or the lateral acceleration, especially in the low-speed flight phase. Furthermore, the control coupling characteristics of the LSR aircraft should be dealt with to avoid roll departure motion occurring

(3) The EA-based controller exhibits a better decoupling performance than the ESO-based controller because the eigenvalues and eigenvectors are assigned simultaneously. However, the complexity of parameter scheduling and the relative weak disturbance rejection capability of EA-based control means that the ESO-based controller is more practical in engineering terms. A large number of simulations and assessments, including flight tests, have demonstrated the effectiveness of the ESO-based controller

Further work will focus on utilizing the disturbance rejection capability of the ESO-based controller and the decoupling characteristics of the EA-based controller. One approach may be to use the MIMO design method for the ESO-based controller. Another method would involve combining the disturbance rejection module of ESO in the EA design process. These aspects require further research to achieve complete and robust decoupling control.

Data Availability

The data used to support the findings of this study are available from the corresponding author upon reasonable request.

Conflicts of Interest

The authors declare that there is no conflict of interest regarding the publication of this paper.

Acknowledgments

This work was supported by the National Defense Science and Technology Foundation Strengthening Program and the Priority Academic Program Development of Jiangsu Higher Education Institutions (PAPD).

References

[1] R. E. Day, *Coupling Dynamics in Aircraft: A Historical Perspective, Vol. 532*, Scientific and Technical Information Program, National Aeronautics and Space Administration, Office of Management, 1997.

[2] D. Wang, J.-F. Wang, L.-F. Li, T.-P. Yang, and J.-T. Chen, "Novel volume-improved design method of large-slenderness-ratio cone-derived waveriders," *AIAA Journal*, vol. 58, no. 11, pp. 4832–4847, 2020.

[3] M. T. Moul and J. W. Paulson, "Dynamic lateral behavior of high-performance aircraft," in *NACA Conference on High-speed Aerodynamics*, Langley Field, 1958.

[4] F. H. Lutze, W. C. Durham, and W. H. Mason, "Unified development of lateral-directional departure criteria," *Journal of Guidance, Control, and Dynamics*, vol. 19, no. 2, pp. 489–493, 1996.

[5] R. Weissman, "Development of design criteria for predicting departure characteristics and spin susceptibility of fighter-type aircraft," in *2nd Atmospheric Flight Mechanics Conference*, Palo Alto,CA,USA, 1972.

[6] R. Weissman, "Preliminary criteria for predicting departure characteristics/spin susceptibility of fighter-type aircraft," *Journal of Aircraft*, vol. 10, no. 4, pp. 214–219, 1973.

[7] X. Li, Y. Yang, Q. He, Z. Cheng, Y. Wang, and L. Liu, "Attitude coupling control and lateral stability analysis of hypersonic vehicle," *2020 Chinese Control And Decision Conference (CCDC)*, 2020, Hefei, China, 2020.

[8] B. Lee, L. Zaichik, Y. Yashin, V. Perebatov, and V. Rodchenko, "Criterion to estimate optimum lateral static stability margin," in *AIAA Atmospheric Flight Mechanics Conference and Exhibit*, Hilton Head, South Carolina, 2007.

[9] Z. T. Dydek, A. M. Annaswamy, and E. Lavretsky, "Adaptive control and the NASA X-15-3 flight revisited," *IEEE Control Systems Magazine*, vol. 30, no. 3, pp. 32–48, 2010.

[10] J. S. Orr and C. J. Dennehy, "Analysis of the X-15 flight 3-65-97 divergent limit-cycle oscillation," *Journal of Aircraft*, vol. 54, no. 1, pp. 135–148, 2017.

[11] A. Snell, "Decoupling control design with applications to flight," *Journal of Guidance, Control, and Dynamics*, vol. 21, no. 4, pp. 647–655, 1998.

[12] P. Acquatella, W. Falkena, E.-J. van Kampen, and Q. P. Chu, "Robust nonlinear spacecraft attitude control using incremental nonlinear dynamic inversion," in *AIAA Guidance, Navigation, and Control Conference*, Minneapolis, Minnesota, 2012.

[13] G. Di Francesco and M. Mattei, "Modeling and incremental nonlinear dynamic inversion control of a novel unmanned tiltrotor," *Journal of Aircraft*, vol. 53, no. 1, pp. 73–86, 2016.

[14] W. L. Garrard, "Lateral directional aircraft control using eigenstructure assignment," *Journal of Guidance, Control, and Dynamics*, vol. 21, no. 3, pp. 523–525, 1998.

[15] K. M. Sobel and E. Shapiro, "Eigenstructure assignment for design of multimode flight control systems," *IEEE Control Systems Magazine*, vol. 5, no. 2, pp. 9–15, 1985.

[16] L. Wang, N. Zhang, Y. U. Ting, L. I. Hailiang, Z. H. Jianghui, and J. I. Xiaopeng, "Three-axis coupled flight control law design for flying wing aircraft using eigenstructure assignment method," *Chinese Journal of Aeronautics*, vol. 33, no. 10, pp. 2510–2526, 2020.

[17] C. Nieto-Wire and K. Sobel, "Eigenstructure assignment for a tailless aircraft," *AIAA Guidance, Navigation and Control Conference and Exhibit*, Hilton Head, South Carolina, 2007.

[18] B. Nie, Z. Liu, F. Cen, D. Liu, H. Ma, and O. Sename, "An innovative experimental approach to lateral-directional flying quality investigation for tailless aircraft," *IEEE Access*, vol. 8, pp. 109543–109556, 2020.

[19] J. Han, "Active disturbance rejection controller and its applications," *Control and Decision*, vol. 13, no. 1, pp. 19–23, 1998.

[20] J. Chen, D. Nannan, and Y. Han, "Decoupling attitude control of a hypersonic glide vehicle based on a nonlinear extended state observer," *International Journal of Aerospace Engineering*, vol. 2020, Article ID 4905698, 11 pages, 2020.

[21] Y. Wu and J. Wang, "Continuous recursive sliding mode control for hypersonic flight vehicle with extended disturbance

observer," *Mathematical Problems in Engineering*, vol. 2015, Article ID 506906, 26 pages, 2015.

[22] W. Liu, C.-A. Zhang, X.-P. Wang, J.-J. Li, and F.-M. Wang, "Parametric study on lateral–directional stability of hypersonic waverider," *AIAA Journal*, vol. 59, no. 8, pp. 3025–3042, 2021.

[23] J. R. Chambers and R. M. Hall, "Historical review of uncommanded lateral-directional motions at transonic conditions," *Journal of Aircraft*, vol. 41, no. 3, pp. 436–447, 2004.

[24] C.-s. Kim, T. Jin, G.-o. Koh, and B. s. Kim, "Control law design to improve the unexpected pitch motion in slow down turn maneuver," *Proceedings of the Institution of Mechanical Engineers, Part G: Journal of Aerospace Engineering*, vol. 236, no. 1, pp. 123–139, 2022.

[25] R. L. Bisplinghoff and H. Ashley, "Principles of aeroelasticity," *Courier Corporation*, 2013.

[26] H. Lee, M. Chang, and M. Kaiser, "Flight dynamics and stability and control characteristics of the X-33 technology demonstrator vehicle," in *Guidance, Navigation, and Control Conference and Exhibit*, Boston, MA, USA, 1998.

[27] C. Breitsamter, T. Cvrlje, B. Laschka, M. Heller, and G. Sachs, "Lateral-directional coupling and unsteady aerodynamic effects of hypersonic vehicles," *Journal of Spacecraft and Rockets*, vol. 38, no. 2, pp. 159–167, 2001.

[28] Military specification flying qualities of piloted airplanes, *MIL-F-8785C*, MIL Standard and Handbook, Washington, DC, 1991.

[29] B. L. Stevens, F. L. Lewis, and E. N. Johnson, *Aircraft Control and Simulation: Dynamics, Controls Design, and Autonomous Systems*, John Wiley & Sons, 2015.

[30] S. Srinathkumar, "Eigenvalue/eigenvector assignment using output feedback," *IEEE Transactions on Automatic Control*, vol. 23, no. 1, pp. 79–81, 1978.

[31] J. Li, Y. Xia, X. Qi, and Z. Gao, "On the necessity, scheme, and basis of the linear–nonlinear switching in active disturbance rejection control," *IEEE Transactions on Industrial Electronics*, vol. 64, no. 2, pp. 1425–1435, 2017.

[32] Z. Gao, "Scaling and bandwidth-parameterization based controller tuning," *Proceedings of the American Control Conference*, vol. 6, 2006.

[33] Z.-H. Wu and B.-Z. Guo, "Extended state observer for MIMO nonlinear systems with stochastic uncertainties," *International Journal of Control*, vol. 93, no. 3, pp. 424–436, 2020.

[34] B.-Z. Guo and Z.-l. Zhao, "On the convergence of an extended state observer for nonlinear systems with uncertainty," *Systems & Control Letters*, vol. 60, no. 6, pp. 420–430, 2011.

[35] J. Han, *Active Disturbance Rejection Control Technique-the Technique for Estimating and Compensating the Uncertainties*, National Defense Industry Press, Beijing, 2008.

[36] J. Puig-Navarro, K. Ackerman, N. Hovakimyan et al., "An L1 adaptive stability augmentation system designed for *MIL-HDBK-1797* level 1 flying qualities," in *AIAA Scitech 2019 Forum*, San Diego, California, 2019.

[37] M. Bodson, "Evaluation of optimization methods for control allocation," *Journal of Guidance, Control, and Dynamics*, vol. 25, no. 4, pp. 703–711, 2002.

[38] C. Nieto-Wire and K. Sobel, "Flight control design for a tailless aircraft using eigenstructure assignment," *International Journal of Aerospace Engineering*, vol. 2011, Article ID 549131, 13 pages, 2011.

[39] B. Bergeon, *Robust Modal Control with a Toolbox for Use with Matlab®*, J. F. Magni, Ed., Kluwer Academic/Plenum Publishers, New York, NY, 2003.

[40] D. Shao, X. Sichuan, and D. Aimin, "Absolute stability analysis of nonlinear active disturbance rejection control for electromagnetic valve actuator system via linear matrix inequality method," *Proceedings of the Institution of Mechanical Engineers, Part I: Journal of Systems and Control Engineering*, vol. 232, no. 9, pp. 1134–1145, 2018.

[41] A. M. J. Olsson and G. E. Sandberg, "Latin hypercube sampling for stochastic finite element analysis," *Journal of Engineering Mechanics*, vol. 128, no. 1, pp. 121–125, 2002.